ORIGINAL REPORT

Fluid effects in model granular flows

Yuting Zhao[1] · W. Andy Take[2] · Roland Kaitna[3] · Brian W. McArdell[4] · Jim N. McElwaine[5] ·
Elisabeth T. Bowman[1]

Abstract

Pore fluid plays a crucial role in many granular flows, especially those in geophysical settings. However, the transition in behaviour between dry flows and fully saturated flows and the underlying physics that relate to this are poorly understood. In this paper, we report the results of small-scale flume experiments using monodisperse granular particles with varying water content and volume in which the basal pore pressure, total pressure, flow height and velocity profile were measured at a section. We compare the results with theoretical profiles for granular flow and with flow regimes based on dimensional analysis. The runout and the centre of mass were also calculated from the deposit surface profiles. As the initial water content by mass was increased from zero to around 10%, we first observed a drop in mobility by approximately 50%, as surface tension caused cohesive behaviour due to matric suction. As the water content was further increased up to 45%, the mobility also increased dramatically, with increased flow velocity up to 50%, increased runout distance up to 240% and reduced travel angle by up to 10° compared to the dry case. These effects can be directly related to the basal pore pressure, with both negative pressures and positive pore pressures being measured relative to atmospheric during the unsteady flow. We find that the initial flow volume plays a role in the development of relative pore pressure, such that, at a fixed relative water content, larger flows exhibit greater positive pore pressures, greater velocities and greater relative runout distances. This aligns with many other granular experiments and field observations. Our findings suggest that the fundamental role of the pore fluid is to reduce frictional contact forces between grains thus increasing flow velocity and bulk mobility. While this can occur by the development of excess pore pressure, it can also occur where the positive pore pressure is not in excess of hydrostatic, as shown here, since buoyancy and lubrication alone will reduce frictional forces.

Keywords Granular flow · Chute flow · Multiphase flow · Flume experiment · PIV · Pore pressure

List of symbols

h	Local flow height normal to the flume bed, m
L	Travel distance calculated from the flume end, m
n	Porosity, $1 - v_s$
N_{Sav}	Savage number
N_{Bag}	Bagnold number
N_{fric}	Friction number
p_t	Basal total pressure or normal stress [Pa]
p_w	Basal pore water pressure, Pa
p_{st}	Steady-state fluid pressure at bed, Pa
p'	Effective basal normal stress, Pa
t	Time, s
u	Local flow velocity, m/s
u_{ave}	Depth-averaged flow velocity, m/s
u_{slip}	Slip velocity, m/s
u_{surf}	Surface velocity, m/s
V_{bulk}	Bulk solid volume, L
w	Water content
w_0	Saturation water content at static state
w_x	Boundary water content
α_T	Travel angle, °
β	Boundary velocity ratio
$\dot{\gamma}$	Local shear rate, 1/s

✉ Elisabeth T. Bowman
e.bowman@sheffield.ac.uk

1 Department of Civil and Structural Engineering, University of Sheffield, Sheffield, UK

2 Department of Civil Engineering, Queen's University at 16 Kingston, Kingston, Canada

3 University of Natural Resources and Life Sciences, Vienna, Austria

4 Swiss Federal Institute for Forest, Snow and Landscape Research (WSL), Zurich, Switzerland

5 Department of Earth Sciences, Durham University, Durham, UK

δ Grain diameter, m
η Dynamic viscosity of pore fluid, Pa·s
θ Slope angle, °
ρ_s Solid density, kg/m^3
ρ_w Water density, kg/m^3
v_s Solid volume fraction, 1-n

1 Introduction

Granular flows universally exist in nature and are of concern within multiple fields including geophysical contexts (e.g. debris flows, rock avalanches and sediment transport) and industrial contexts (e.g. powder technology, pharmaceuticals and hydrocarbon extraction). The behaviour of dense dry granular flow down an inclined plane has been widely studied and some of its most significant physical characteristics have been revealed. For instance: Louge [1] proposed a model that considers granular flow stresses to be the superposition of a collisional contribution, which depends on flow rate, and a frictional contribution, which is independent of flow rate but dependent on pressure; GDR MiDi [2] quantitatively compares granular flows down an inclined plane with flows in other configurations; Jop, et al. [3] proposed the well-known μ(I) rheology that has led to many following works; Kumaran [4] developed an analysis approach to granular flow dynamics based on kinetic theory; Gray, et al. [5] investigated the mechanism of grain size segregation in non-uniform granular flows. The prevailing research on granular flow behaviours, including the aforementioned works, adopts the dry flow condition (Fig. 1 – "Dry").

The behaviour of granular flows in nature is made considerably complex by the existence of a viscous pore fluid through different mechanisms which depend on the moisture content. A small amount of pore fluid added to a granular body forms liquid bridges between the wetted solid grains (Fig. 1 – "Undersaturated"), generating a cohesion which enhances the shear strength [6] and tensile strength [7] of the unsaturated granular mass due to the tension in the liquid bridges. This cohesion is related to "matric suction" that connects the saturation degree with the shear strength of unsaturated soil [8]. However, although cohesion or matric suction (primarily caused by surface tension at low water content) [9] and negative relative pore pressure (primarily cause by dilation) [10] are theoretically considered to affect bulk dynamics [11] and flow mobility [12], there is yet to be a direct determination of their impact on the macroscopic behaviour of granular flows.

When liquid pore fluid is sufficient to fill up the interstitial spaces or immerse the solid grains, grains under dense flow conditions are subject to hydrodynamic interactions, although intergranular contacts remain non-trivial as otherwise the dilute flowing mass would be considered a granular suspension [13, 14]. Here, we depict two possibilities in Fig. 1 – "Saturated", where water is just available to fill the pore space under a static or dense flow and "Oversaturated", where additional water is available to enable particle mixtures to dilate or expand without air entering the void space. Observations on geophysical granular flows show that, in contrast to dry flows such as rockfalls, saturated flows such as debris flows, lahars and hyperconcentrated flows can travel over much greater distances and maintain their speed even on very low angle slopes [15]; this phenomenon is typically attributed to the development and sustaining of pore fluid pressure [16], as the pore pressure in a flow decreases the normal effective stress between solid grains and the basal surface, and thus also the shear resistance since it is primarily due to frictional forces. This much is uncontroversial, but what controls the development of pore pressure is a matter of debate: several developing mechanisms of non-hydrostatic pore pressure have been discussed in Kaitna, et al. [17] and different models determine the pore pressure in different ways, e.g. Kowalski and McElwaine [18], Iverson and George [19], Bouchut, et al. [20]. There has also been recent work demonstrating the significant effects of moisture in direct simulations of granular flow impact [21]. Despite this, there seems no published experimental study at present focusing on granular flow behaviour in response to different moisture conditions on a continuum from dry to oversaturated.
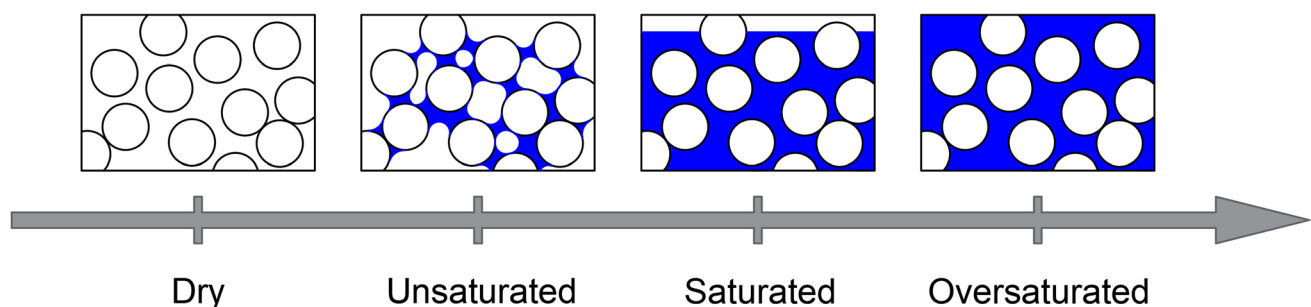

Fig. 1 Schematic diagram of granular flows in different moisture conditions from dry to oversaturated

To understand better pore fluid effects in granular flows, we have performed small-scale flume or chute experiments where the input volumes of solid and fluids were controlled and basal total pressure, basal pore pressure, flow thickness, flow velocity and flow deposit data were measured; such systematic control and careful measurement of these parameters (especially pore pressure) are only available in laboratory experiments. We present here straightforward relationships between simple test inputs (i.e. source volume and water content) and macroscopic outputs of interest (i.e. pore pressure, velocity and mobility) that reveal the fundamental role of pore fluid in granular flow dynamics. We finally discuss

how pore fluid pressure affects the internal flow dynamics and bulk flow mobility in a quantifiable manner.

2 Methods

2.1 Small-scale flume arrangement

The small-scale flume system used in this study is shown in Fig. 2. The inclined part of the flume is 1.4 m long and 0.1 m wide, and was set to an angle of 30°; this connects to a horizontal channel of the same width. All components aside from the metal hopper, which was chosen for
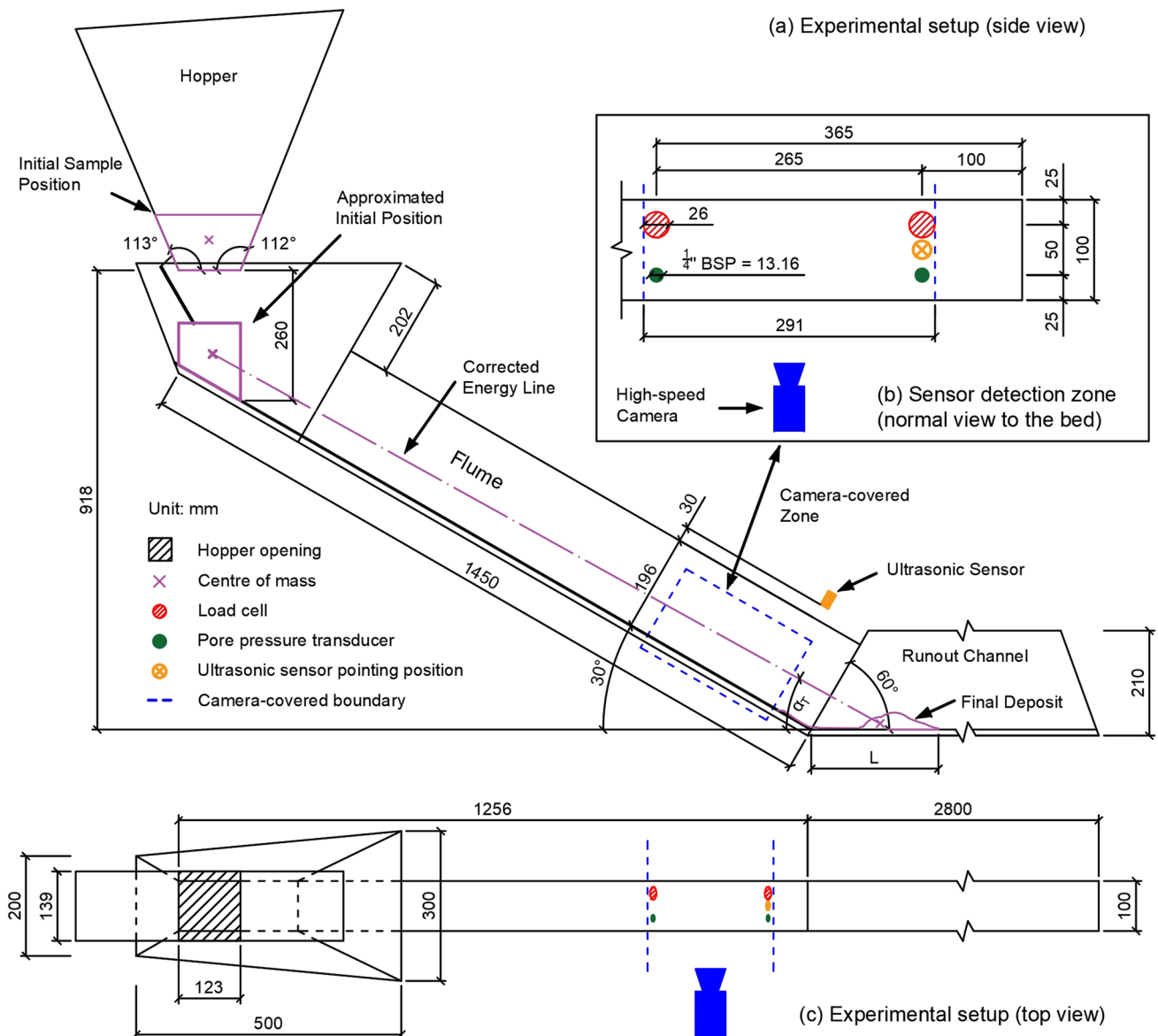

Fig. 2 **a** Experimental setup (side view) in which travel distance (L) and travel angle (α_T) are marked. **b** Zoomed-in data sensor detection zone (normal view to the bed). **c** Experimental setup (top view). All measurements are given in mm

the convenience of sealing the opening and enabling agitation of the source material, are manufactured from clear acrylic to allow easy observation and measurement; the base of the inclined flume is covered with a layer of roughened aluminium while that of the horizontal channel is not. A loadcell (LC) and pore pressure transducer (PPT) pair are mounted within the base of the inclined flume at an "upslope position", 365 mm from the flume end and another at a "downslope position", 100 mm from the end. An ultrasonic sensor is mounted above the downstream end, as shown in Fig. 2b. LCs utilised in the experimental work are Compact Tension/Compression model LUX-B-ID by Kyowa at a rated capacity of ± 50 N; PPTs are Druck model PDCR with a measurement range of ± 35 kPa; the ultrasonic sensor is model S18UUAQ by Banner Engineering. Each PPT is saturated with de-aired water before conducting a test and is capped flush with a metal mesh of 0.5 mm aperture to prevent solids from directly touching the fluid inside the PPT hole and interfering with sensor response.

Sensor signals were collected at a frequency of 36 kHz with data subsequently filtered and averaged to reduce noise. A Phantom Miro 310 high-speed camera was located near the flume outlet, aimed between the sensor-mounted zone to capture a planar side view of the flow at both upstream and downstream positions; high-speed images were captured at 1200 fps (frames per second) for dry and fully saturated tests and 3000 fps for wet tests with varying water content.

Two slightly different flume arrangements were used in this study. The first sets of tests involving fully dry flows (results denoted "D") and fully saturated flows (results denoted "S") had four fixing points for the flume slope. The later tests for variable water content (results denoted "W") had 10 fixing points. This led to greater bed rigidity and this had an unexpectedly large influence on the runout behaviour observed (an approximate increase in the horizontal centre of mass of 20% for the deposits). Therefore, the results can be directly compared between D and S tests; while W tests should be considered as a separate suite, albeit with comparable trends.

2.2 Materials

The solid material selected for granular flow experiments is the 3 mm nominal size Denstone® 2000 Support Media provided by Saint-Gobain Norpro, a product of ceramic pseudo-spheres with an average grain size of $\delta = 3.85$ mm; this product, which has previously been used in Raymond [22], Coombs [23], Taylor-Noonan, et al. [24], is considered suitable for multiple test runs due to its hardness (ensuring particle characteristics do not change between tests), roughness (not explicitly measured but particles are rough to the touch), sphericity and uniformity. The particle

size was also chosen to ensure that excess pore pressure (above hydrostatic) would be unlikely to be produced in wet or saturated tests. The physical properties of the ceramic beads are summarised in Table 1, where different data sources are presented; measured parameters include the average void ratio (thus the saturation water content at rest, denoted as w_0, can be calculated) identified by pouring water into the dry sample sitting inside the hopper (as shown in Fig. 2a) and the flume grain-bed friction angle determined by tilting channel tests, which was measured when a layer of dry grains started to move in a channel of equal width to that of the inclined flume.

Depending on the moisture composition of the sample from fully dry to oversaturated, experiments are categorised into three groups: D for dry tests, S for saturated tests and W for wet tests involving conditions from unsaturated to saturated. Source volume (specifically the bulk volume of the dry sample) is set as the variable for the D and S groups, while the W group is varied in water content; the values of source volume (in litre) and water content (in percentage) used for each test is attached to the test group to constitute each test label. Sample conditions of different test groups are listed in Table 2.

The prepared sample is poured into the hopper at the top of the flume system (Fig. 2a) before being released into the tilted flume. A pneumatically-operated trapdoor is attached to the hopper to seal the opening and to prevent leakage; once the trapdoor is triggered by a microswitch linking to the high-speed camera and sensors, the sample falls from the hopper and synchronously the data acquisition begins. The sample flows downslope, passing through the sensor-mounted zone, and then into the horizontal confined channel before coming to a rest.

Table 1 Physical parameters of experimental solid material. Data are from (a) Coombs [23], (b) Raymond [22], (c) Denstone 2000 datasheet, and (d) measurement or calculation

	Denstone 2000 Beads	Data Source
Grain Density (kg/m³)	2240	a
Nominal Size (mm)	3	c
Diameter (mm)	2.8 – 4.3	c
Average Diameter (mm)	3.85	a
Average Void Ratio	0.575	d
Sphericity (%)	92.2	a
Restitution Coefficient	0.611	a
Internal Friction Angle (°)	33.7	b
Friction Angle on the Aluminium Bed (°)	21	d
Saturation water content at rest	0.256	d

Table 2 Information of experimental source materials. the D and S groups have fixed water content and varying bulk source volume, while the W group has fixed source volume and varying water content

Test Group	Test Label	Bulk Dry Volume (L)	Gravimetric Water Content	Initial Bulk Density (kg/m^3)	Initial Porosity	Initial Solid Volume Fraction
D	D-0.75L-0%	0.75	0	1402	0.374	0.626
	D-1L-0%	1.0		1419	0.368	0.633
	D-1.5L-0%	1.5		1414	0.369	0.631
	D-2L-0%	2.0		1431	0.361	0.639
	D-4L-0%	4.0		1417	0.368	0.632
S	S-0.75L-45%	0.75	0.45	1776	0.374	0.626
	S-1L-45%	1.0		1799	0.355	0.645
	S-1.5L-45%	1.5		1784	0.367	0.633
	S-2L-45%	2.0		1790	0.363	0.638
	S-4L-45%	4.0		1782	0.369	0.631
W	W-2L-1%	2.0	0.01	1447	0.361	0.639
	W-2L-10%		0.10	1569	0.363	0.637
	W-2L-25%		0.25	1637	0.360	0.635
	W-2L-30%		0.30	1793	0.361	0.640
	W-2L-35%		0.35	1792	0.366	0.639
	W-2L-40%		0.40	1786	0.360	0.634

2.3 Data analysis

Data analysis extracted information from the raw experimental data, including sensor signals, high-speed images and manually measured deposit data, through various approaches. Particle Image Velocimetry (PIV), a well-developed and widely-accepted approach, was utilised to produce velocity profiles from high-speed images. The adopted PIV software, GeoPIV, was established by [25] and has been involved in many research works, e.g. Coombs [23], White, et al. [25], Sanvitale and Bowman [26], Gollin, et al. [27]. More details of data processing can be found in Appendix A.

For capturing the flow regime, several dimensionless numbers, namely the Savage number, Bagnold number and friction number, may be used to identify the dominant momentum transfer mechanism. The Savage number (N_{Sav}) for grain-fluid mixtures was presented by Iverson [16] and is defined by the ratio of solid inertial stress to quasi-static solid stress; noting that Savage number and Inertial number [2, 28], which is another commonly-used dimensionless number equivalent to the square root of Savage number, are physically identical but expressed differently. Later in Iverson, et al. [29], a transformed expression suitable for easier measurement at the bed was proposed; using this transformed equation, N_{Sav} is given by:

$$N_{Sav} = \frac{\rho_s \dot{\gamma}^2 \delta^2}{p_t - p_w} \tag{1}$$

in which ρ_s is the solid density, $\dot{\gamma}$ is the local shear rate, δ is the grain size, p_t is total pressure (i.e. total normal stress)

at basal boundary, and p_w is basal pore water pressure. As suggested by Savage and Hutter [30], collisional stresses dominate over frictional stresses borne by sliding and sustained contacts if N_{Sav} exceeds about 0.1.

The Bagnold number (N_{Bag}) is defined as the ratio of solid inertial stress to viscous fluid shear stress [31, 32]; the form of N_{Bag} provided by Iverson [16] is defined by:

$$N_{Bag} = \frac{v_s}{1 - v_s} \cdot \frac{\rho_s \dot{\gamma} \delta^2}{\eta} \tag{2}$$

where v_s is solid volume fraction or solid concentration, which in this study is assumed constant in the flow body, and η is the dynamic viscosity of pore fluid, which is air for dry flows and water for saturated flows (in both S and W groups); the η values at 25 ℃ are selected for both pore fluids. A collision-dominated flow regime is inferred when $N_{Bag} > 200$. Under the unsaturated condition corresponding with $w < w_0 = 0.256$ (Table 1), pore fluid cannot fill up the voids within the source material and tends to adhere to the grain surface or to form liquid bridges between grains; hence the dominant solid–fluid interaction is not viscous shear but "matric suction" or apparent "cohesion". As a result, analysing momentum transfer based on viscous shear stress is not suitable for the unsaturated granular flows and N_{Bag} calculation is then only applied to dry ($w = 0$) and saturated flows ($w \geq w_0$).

The friction number (N_{fric}), which expresses the ratio of shear stress produced by enduring contacts to viscous shear stress, is determined by the ratio of the Bagnold number to the Savage number [33]:

$$N_{\text{fric}} = \frac{N_{\text{Bag}}}{N_{\text{Sav}}} = \frac{v_s}{1 - v_s} \cdot \frac{\sigma_{\text{basal}} - p_{\text{basal}}}{\eta \dot{\gamma}} \qquad (3)$$

Large N_{fric} indicates that solid shear stresses exceed pore fluid viscous shear stresses; a threshold value of about 100 is experimentally determined by [34].

As the 2-D flow path simplifies the analysis by limiting the spread of grains to the flanks, bulk flow mobility in this study is characterised by two parameters: (i) travel distance (L), i.e. the length of the deposit body in the horizontal channel, and (ii) travel angle (α_T), i.e. the angle of the line connecting the Centre of Mass (COM) of the source volume to that of the deposit with the horizontal [35]. The definitions of travel distance (L) and travel angle (α_T) are illustrated in Fig. 2a, in which an approximated initial position of the source material and a corrected energy line is used to

calculate α_T; this is because the fall distance from the hopper to the flume bed contributes little to the flow mobility compared with its effect on the α_T value; the initial sample position in the hopper is not useful and thus the source material is approximated into a trapezoidal block resting on the bed with its centroid being the initial COM, as shown in Fig. 2a. Further details are available in Appendix B.

3 Results

3.1 Flow velocities

Flow velocity profiles at the peak flow height for different tests are given in Fig. 3, where (a–c) depict the PIV-measured velocity data averaged over 0.02 s (discrete symbols), against
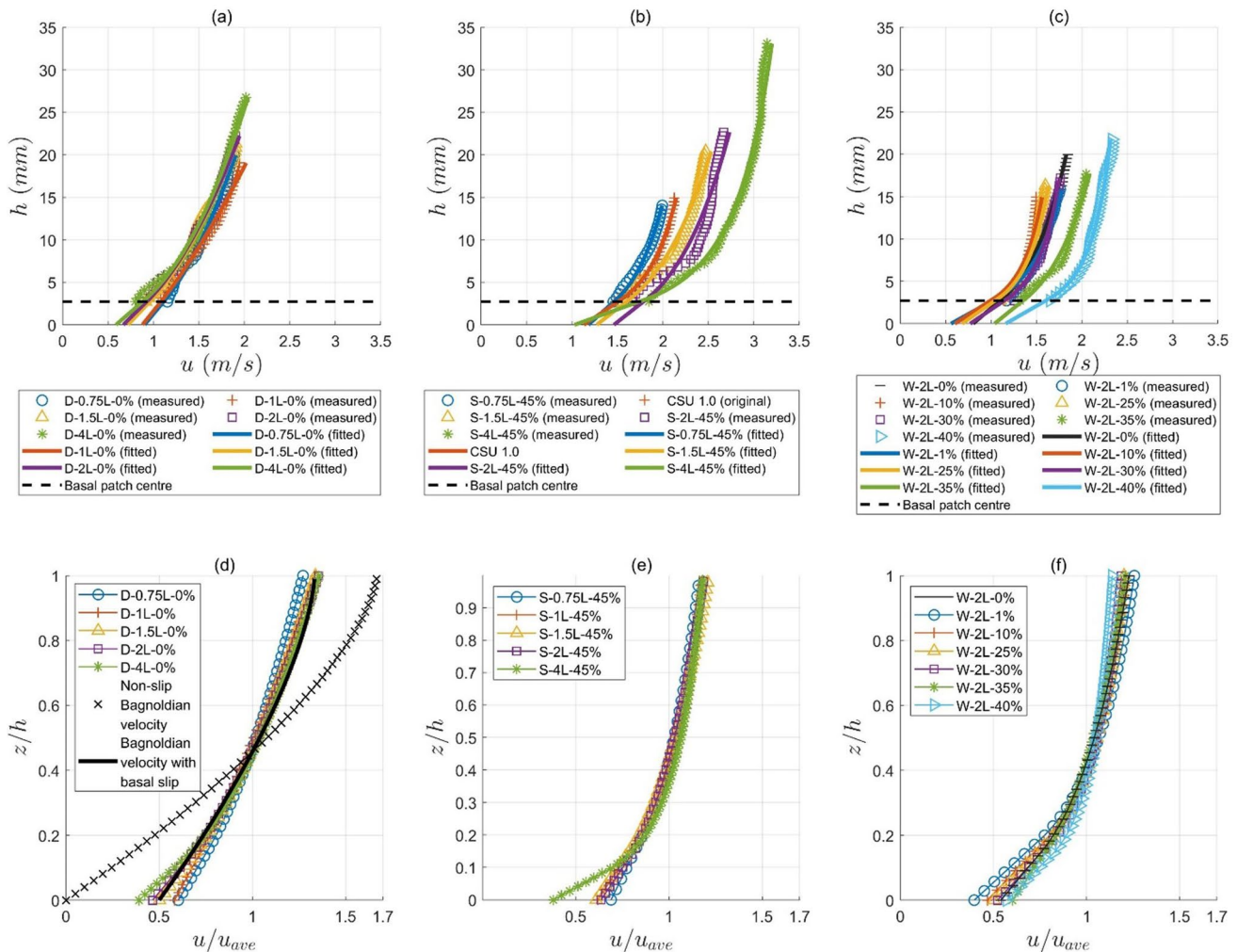

Fig. 3 Flow head velocity profiles of dry flows (left column), saturated flows (0.45 water content, middle column) and wet flows (2L source volume, right column), where (**a–c**) compare the measured velocities (discrete markers) and the fitted velocities (solid curves) against the absolute flow height (**h**), and (**d–f**) the normalised veloci-

ties by depth-averaged velocity (u/u_{ave}) against the normalised flow height (z/h). Black dotted lines represent the lowest position of accurate PIV measurement. Bagnoldian velocity profiles with non-slip boundary and with an assumed normalised slip velocity of $u/u_{\text{ave}} = 0.5$ are both presented in subplot (**d**)

the absolute flow height, along with the power-fitted velocity data (solid curves), and (d–f) show velocity profiles normalised by the depth-averaged velocity against normalised flow height [36].

Black dotted lines in Fig. 3a–c denote the position of the "basal patch centre", below which the accuracy of PIV measurement is not guaranteed; hence from the flume bed ($h=0$) to the dotted line, the measured data are not shown and the fitted data are amended (Appendix A).

Velocity profiles of dry flows in our experiments are almost linear across the depth and barely vary in magnitude with source volume. In contrast, wet flow velocity profiles, saturated or not, are more curved near the bed and a clear increase in the velocity magnitude with source volume can be found in the upper part of the flow. Larger source volume increases the normalised surface velocity slightly but gives lower normalised slip velocity, and thereby stronger bulk shear across the depth and stronger local shear near the bed; this trend is strengthened by the existence of pore fluid. Additionally, two versions of the classic Bagnoldian velocity profile for steady-uniform dry granular flows in open channels [31, 37] are plotted in Fig. 3d for reference: the Bagnoldian velocity with no slip velocity at a given normalised height, z/h, can be expressed as:

$$u\left(\frac{z}{h}\right) \propto h^{\frac{3}{2}} \cdot \left[1 - \left(1 - \frac{z}{h}\right)^{\frac{3}{2}}\right] \tag{4}$$

whereas the modified version with an assumed normalised slip velocity $u/u_{\mathrm{ave}} = 0.5$ at $z=0$ is also calculated as follows to be comparable with the tested dry flows:

$$u\left(\frac{z}{h}\right) \propto h^{\frac{3}{2}} \cdot \left[\frac{8}{5} - \left(1 - \frac{z}{h}\right)^{\frac{3}{2}}\right] \tag{5}$$

As shown in Fig. 3d, the normalised power-fitted velocity profiles of the tested dry flows are in good agreement with the modified Bagnoldian profile but give notably weaker bulk shear compared with the original non-slip version. Considering that the difference between the surface and slip velocities tends to increase with source volume, it seems possible that the velocity profile of the tested dry flows can approach the non-slip Bagnoldian profile, given a sufficiently large source volume or flow thickness.

For the tested wet flows, except for the almost-dry case of $w=0.01$ which gives larger velocity than that of the $w=0.1$ unsaturated flow, higher water content increases the velocity magnitude over the entire flow depth, but increases normalised slip velocity and decreases normalised surface velocity, generating weaker shear with greater basal slip. Contrasting with those of dry flows, the normalised velocity profiles of wet granular flows are less inclined in the upper part and more curved near the bed; the increase in source volume and water content both amplify this effect, producing velocity curves with reduced shear in the upper part of the profile.

Depth-averaged velocities are shown in Fig. 4. The averaging of velocities in this way indicates the importance of the addition of fluid from dry through to oversaturated and how this affects flow rheology. Here it is noted that dry flows (Fig. 4a) maintain the same depth-averaged velocity, irrespective of source volume, decaying over time (i.e. as the tail is reached); in contrast, depth-averaged velocities of highly saturated flows (Fig. 4b) demonstrate a notable increase with source volume. These velocities also reduce rapidly towards tail ends of the flows, although there is no collapse of the data with respect to time and the tails are actually slower than for the dry tests. The reason for this is thought to be that the saturated tests (W series at $w>0.35$ and all S series), tend to have more material travelling fast at the front with larger slip velocity and effectively run out of material in the tail more rapidly than dry flows, so that they
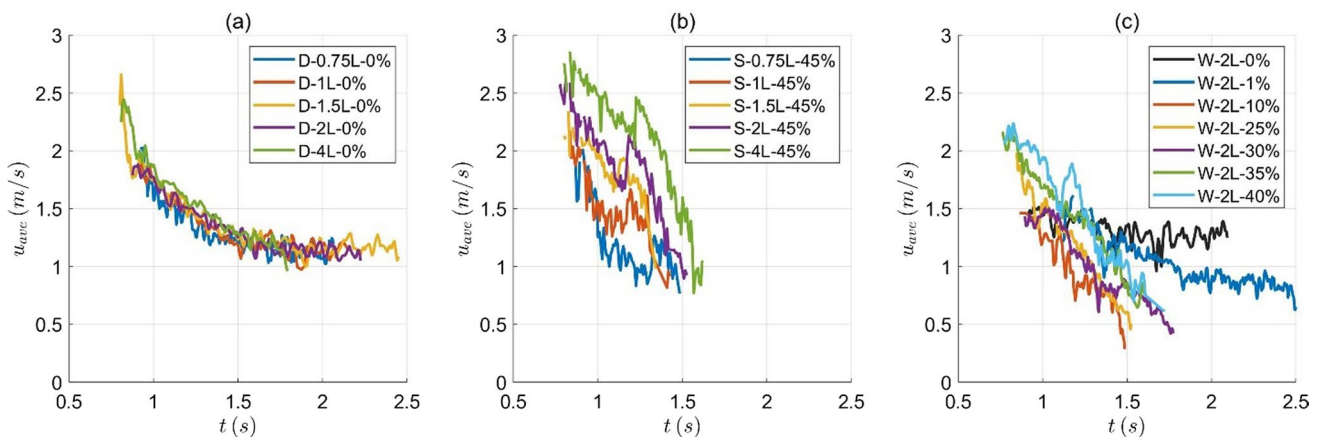

Fig. 4 Depth-averaged velocities of **a** dry flows, **b** saturated flows (0.45 water content) and **c** wet flows (2L source volume)

slow down more rapidly. W series flows at low water content (about $w \leq 0.3$) for the same volume (Fig. 4c) give relatively similar depth-averaged velocities that are lower than for the dry or highly saturated flows, especially in the tails. Flows at a higher water content show clear velocity growth with the added fluid so that W-2L-40% behaves similarly to S-2L-45% in Fig. 4b.

3.2 Flow heights

Flow heights over time of different tests are plotted in Fig. 5a–c, in which the "main surge" part of the flow, excluding the precursory grains, is represented by solid curves and flow tail by dashed lines. The main surge is the focus of the local-scale analyses as it contains most of the flow material and contributes most to the runout, while the thin slow and lengthy flow tail, with thickness of commonly 1–3 grains, is neglected. The end of the main surge is identified when (i) grains stop moving (e.g. piling up as in D-4L-0% or stuck on the bed as in W-2L-10%) or (ii) either the flow height or the basal total pressure hits its minimum value after the peak flow height, depending on which one is reached earlier.

As shown in Fig. 5, across all tests, larger source volume produces larger flow height. Dry flow heights (Fig. 5a) are

relatively evenly maintained over time, whereas saturated flows (Fig. 5b) have thicker and faster main surges and thinner tails. For the W test group (Fig. 5c), the flow height gradually evolves with increasing water content between 0.1 and 0.4, from being similar to that of dry flows into the behaviour of saturated flows – that is, there is no abrupt transition from unsaturated to saturated behaviour.

3.3 Visible water in saturated flows

Figure 6 shows a typical saturated flow where a visible water surface intersects with the top surface of the granular flow at the PIV mesh zone. Before this point, the water surface is likely to be below the granular flow top. In subsequent figures (Figs. 7 and 8), this position is indicated by a red circle in the time series.

For all of the saturated tests, carried out at a water content of 0.45, denoted 'S', and variable water content tests 'W' tests with water content above 0.35, surface water become visible at some point. In other flows, no water surface was observed to spill out of the granular body throughout the main surge. These flows are all of the dry tests denoted 'D' and the wet tests, 'W' at a moisture content of 0.3 or less.
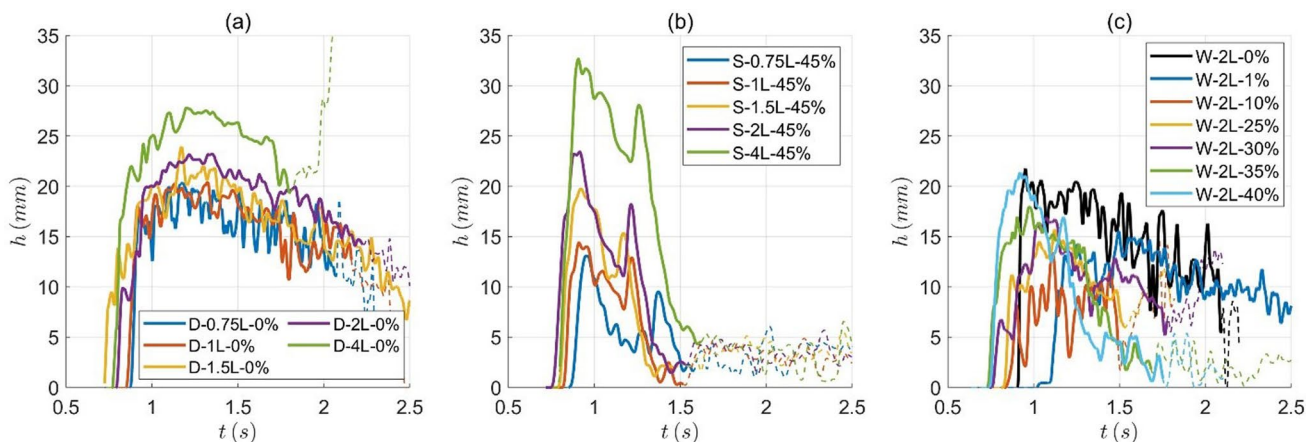

Fig. 5 Flow height evolution with time of **a** dry flows, **b** saturated flows (0.45 water content) and **c** wet flows (2L source volume), in which solid lines represent the main surge part and dash lines the precursory grains and flow tail
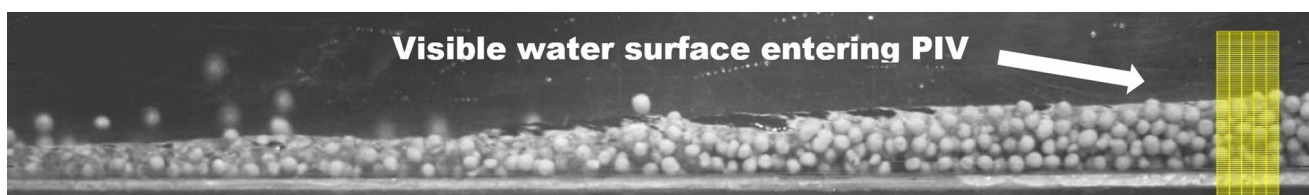

Fig. 6 The frame corresponding with where the visible water surface intersects the flow top surface at the PIV mesh (indicated by a red solid circle in Figs. 7 and 8)
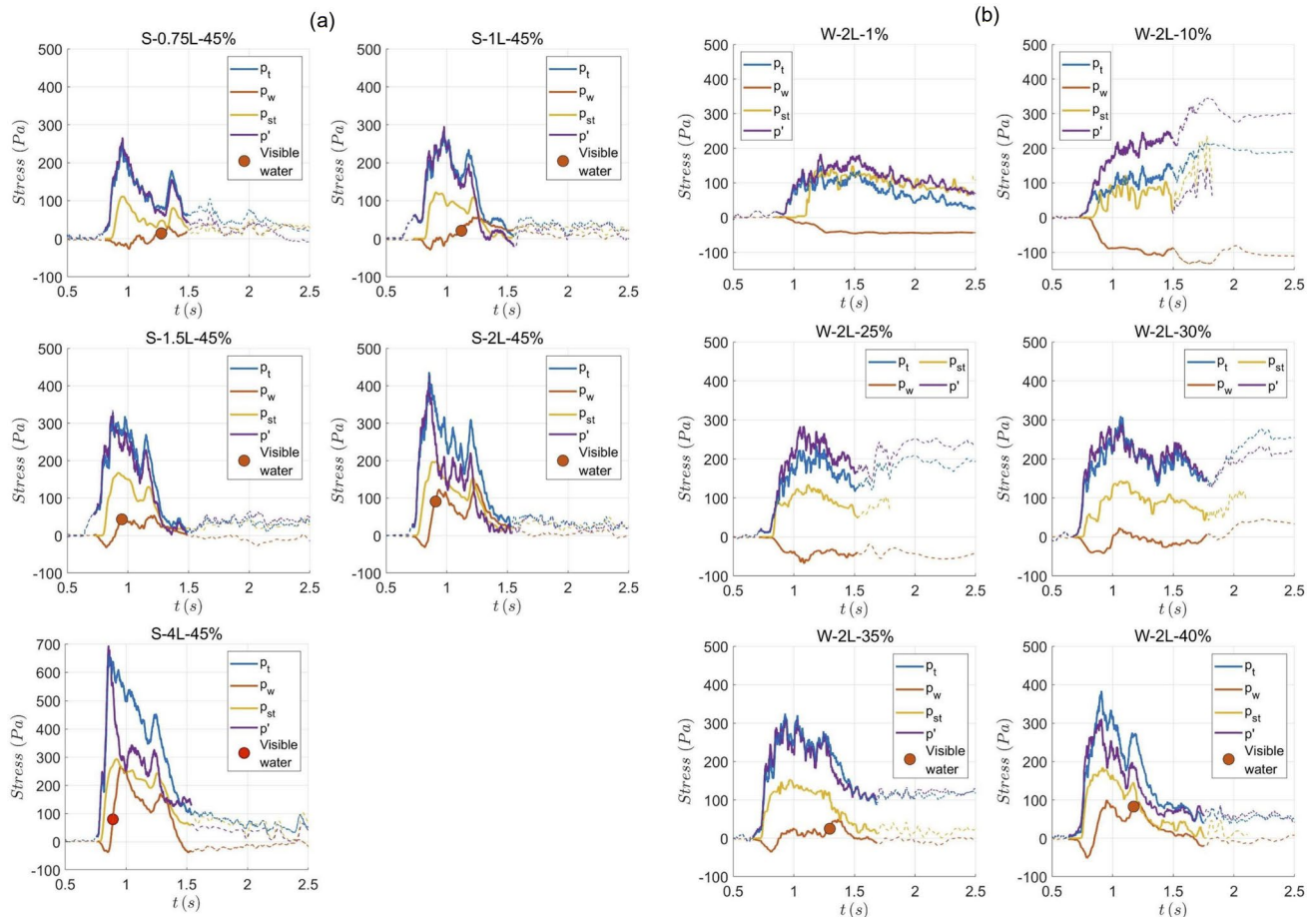
Fig. 7 Comparisons of downslope basal total pressures (p_t), downslope basal pore pressures (p_w), estimated steady-flow fluid pressures (p_{st}) and downslope basal effective stresses (p') of **a** saturated flows (0.45 water content) and **b** wet flows (2L source volume), in which solid lines denote the main surge, dashed lines the other parts of the flow, and red solid circles the time where a visible water surface starts to enter the PIV-detected zone. The downslope position is 100 mm from the flume end

3.4 Total pressures and pore pressures

Stress comparisons among basal total pressure (p_t), basal pore pressure (p_w), estimated steady-state pore pressure (p_{st}), and basal effective stress (p') for wet granular flows are given in Fig. 7 at the downslope position (the upslope position being similar). Subplots (a) and (b) respectively show the stresses of the tested saturated flows (variable source volume) and wet tests (variable water content), and solid lines correspond with the main surge presented in Fig. 5 while dashed lines indicate the precursory grains and flow tail. The fluid pressure estimated under flow conditions that are approximated to be steady is:

$$p_{st} = \rho_w gh cos\theta \qquad (6)$$

where ρ_w is the water density and θ is the slope angle (30°); note that the use of the flow height h presumes a water surface identical to the flow top surface, i.e. the saturation state throughout the flow, and hence, this measure tends to overestimate the pressure value. The basal effective stress is estimated as:

$$p' = p_t - p_w \qquad (7)$$

noting that the basal sensors for the total and pore pressure are located at the same position longitudinally but 50 mm by centre distance from each other laterally (Fig. 2b).

The basal total pressure, p_t, consistently grows with both source volume and water content, whereas the basal pore pressure p_w shows more complex behaviour: (i) p_w always starts negative as the unsaturated flow front arrives and can increase sharply just behind the granular front if the volume is comparatively large or the moisture content relatively high, otherwise it may increase more slowly, (ii) negative rather than positive pressures can dominate the main surge when the source volume or water content is relatively small (e.g. S-0.75L-45% and W-2L-25%), (iii)
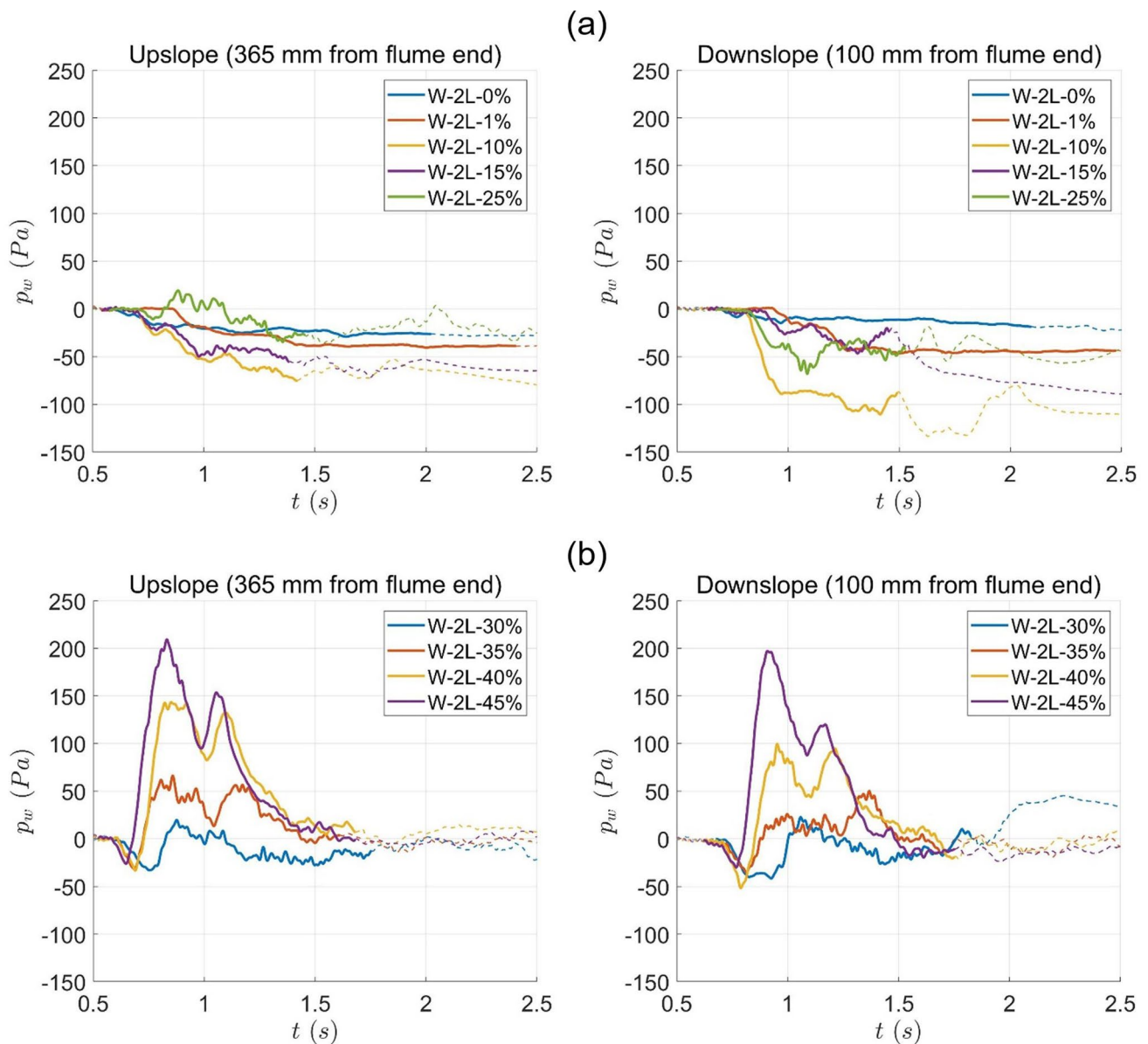
(a)

(b)

Fig. 8 Comparisons between upslope (365 mm from the flume end) and downslope (100 mm from the flume end) pore pressures of **a** flows with less than 0.3 water content, and **b** flows with more than 0.3 water content for 2L initial source volume

p_w rarely exceeds p_st and is always small relative to p_t (lower than a half), suggesting that no excess pore pressure occurs in the experiments.

The position of each red solid circle on the time axes in Fig. 7a and b represents the moment where a visible water surface intersects with the top surface of granular flow at each PIV-analysed zone (Fig. 6). Before this, the water surface is likely to be below the flow top. It is notable that after the appearance of water at the flow surface, p_w stays positive until near the flow tail; if the red circle is not shown, no water surface is observed. The positions of red circles show that, with larger water content and/or source volume, the visible water surface becomes closer to

the leading edge, indicating a higher degree of saturation of the flow head.

The time evolution of basal pore pressure p_w for wet flows at the upslope and downslope positions are shown in Fig. 8a and b. As water content w grows from 0 to 0.25, p_w distribution in the main surge is dominated by negative values; within this range, negative p_w (implying matric suction stress) becomes stronger until about $w = 0.10$ and is then gradually weakened. After $w \geq 0.3$, p_w starts to return positive responses that consistently increase with water content. Negative pressure recorded in a dry flow (W-2L-0%) has been seen to be due to dry grains pulling water from the PPT hole as they roll or slide over; however, a small amount

of moisture in the flow can produce greater negative pressure, showing that matric suction is applied to the bed by the unsaturated granular body. Additionally, the upslope position commonly gives smaller magnitudes of negative pressure and larger positive pressures than the downslope one; this may result from the dilation of the wet granular flow, i.e. the flow becomes more dilute as the solid volume fraction decreases, throughout the downslope motion.

3.5 Dimensionless numbers

Three dimensionless numbers, i.e. the Savage number (N_{Sav}), Bagnold number (N_{Bag}) and friction number (N_{fric}), were derived from fitted velocity profiles to demonstrate the influence of pore fluid on granular flow mechanisms. Figure 9 shows local values of N_{Sav} against normalised flow height z/h and the mean values across the flow depth, $\overline{N}_{Sav}$, against flow height normalised by grain size, h/δ, in subplots (a) and (c), respectively, for dry and saturated flows (variable source volume), and in (b) and (d) for wet flows (variable water content). For each tested flow, the local N_{Sav} data are determined at the peak flow height, while the $\overline{N}_{Sav}$ data are taken after the peak flow height until the end of the main surge, i.e. neglecting the leading edge of each flow. Note that profiles of these numbers are computed from the velocities averaged over 0.02 s as presented earlier. The N_{Sav} profiles of all the tested flows show smaller values in the middle of the flow depth and larger values close to the free surface and bed. For dry flows, N_{Sav} near the flow surface tend to exceed those near the bed, indicating that grains at the free surface are subject to stronger solid inertia than those at the bottom layer; this is opposite to the saturated and wet flows containing pore fluid, in which grains near the bed present greater effect of solid inertia. Visual observation agrees with this difference: the basal layer of wet grains appears to saltate collisionally, although the amplitude of saltation relative to translational movement is reduced as the flow thickness increases, whereas that of dry flows tends translate at a lower velocity than at the surface. The magnitude of N_{Sav} throughout the depth generally decreases with both source volume and water content, showing an increased importance of solid friction compared with solid inertia.

Mean values $\overline{N}_{Sav}$ in all tests, whether varying in source volume (Fig. 9c) or water content (Fig. 9d), give similar reducing trends with increasing h/δ and thus, indicate stronger solid frictional particle contact with thicker flows; the exception is in the thin and slow tails ($h/\delta \leq 2$) of the saturated flows (S series), in which the slip velocity is relatively higher and shear rate lower (hence $\overline{N}_{Sav}$ is lower) than for the wet flows at similar water content and volume (W series). All else being equal, the potential for greater flume vibration in the earlier S series may be responsible for this, although it is not certain. Excluding

data below $h/\delta \leq 2$ in Fig. 9c, $\overline{N}_{Sav}$ data from the dry flows roughly overlap each other at the same h/δ, while those from saturated flows slightly increase with source volume. The result is that $\overline{N}_{Sav}$ of saturated flows at low bulk volume (0.75L to 2L) is approximately an order of magnitude lower than that of dry flows, but for 4L flows, $\overline{N}_{Sav}$ is approximately the same. The implication is that the increased source volume does not cause notable difference in the momentum transport within dry flows, but tends to facilitate the inertial movement of grains in saturated flows. The reason for this may be seen in Fig. 7a, where, for larger source volume flows, increasingly positive pore pressure at the flume bed leads to a reduction in the effective stress, which corresponds to a reduced level of enduring intergranular contact.

For wet flows, $\overline{N}_{Sav}$ decreases with increased water content when $w \leq 0.3$, showing that the flows grow more frictional, but then increases when $w > 0.3$ and reflects a weaker level of enduring intergranular contacts due to the higher degree of saturation of the flow surge; this may be related to the cohesion (matric suction) in the surge when $w = 0.01$–0.3, resulting in a "stickier" flow, thereby strengthening the solid contacts, an effect which is reduced by positive pore pressure when w exceeds 0.3. In addition, all the tested flows are above the threshold value of N_{Sav} and hence are dominated by solid inertia.

Following a similar plotting scheme to that of Fig. 9, Fig. 10 gives the local values of N_{Bag} and N_{fric} in subplot (a) and (b), respectively, and the mean values of $\overline{N}_{Bag}$ and $\overline{N}_{fric}$ in (c) and (d), for dry and saturated flows; the data of wet flows, however, are not shown here due to the involvement of unsaturated conditions and the unclear dependency on the fluid viscous shear stress. The local N_{Bag} values increase monotonically from top to bottom, with the difference between the values at the free surface and the bed for saturated flows being larger than that for dry flows. Conversely, the N_{fric} profiles are larger in the middle and lower at both boundaries. Whether dry or saturated, a larger source volume slightly decreases N_{Bag} in the upper portion and more markedly increases N_{fric} across the flow depth. With the existence of saturating pore fluid, Bagnold number and friction number are greatly reduced in local and mean values, reflecting an enhanced effect of viscous shear stress. In response to an increased normalised flow height beyond $h/\delta = 2$, $\overline{N}_{Bag}$ values do not show clear variations while $\overline{N}_{fric}$ values notably grow larger, showing strengthened solid enduring contacts similar to the results given in Fig. 9c and d. Although the differences in magnitude are not strong, a larger source volume slightly increases $\overline{N}_{Bag}$ but decreases $\overline{N}_{fric}$, indicating that the importance of viscous fluid shear is enhanced relative to solid inertia, but is reduced relative to solid friction.
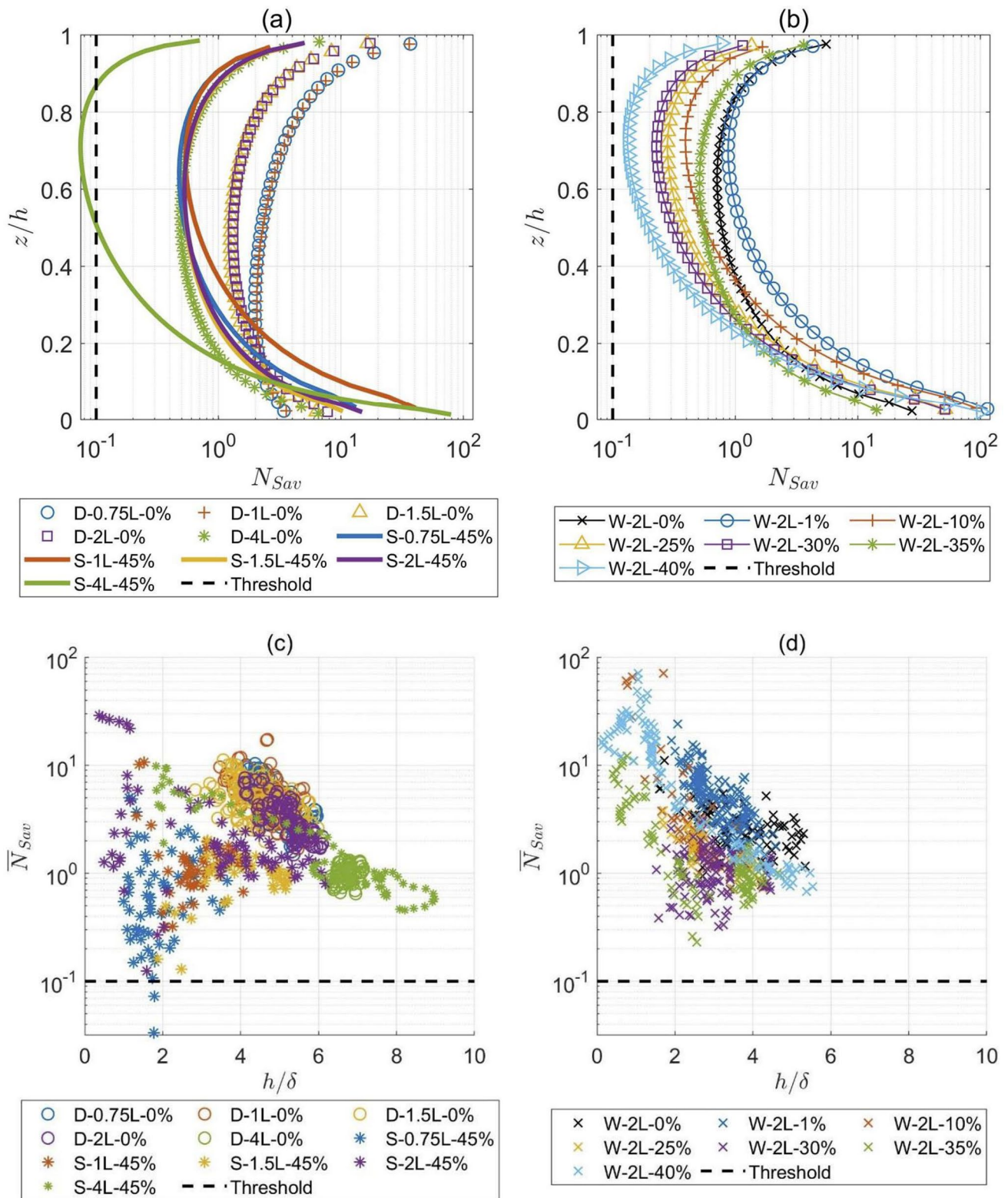
Fig. 9 Local values of Savage number (N_{Sav}) for **a** dry and saturated flows and **b** wet flows against the normalised flow height z/h, where the profile at the peak flow height for each test is plotted. Mean values of Savage number ($\overline{N}_{Sav}$) across the depth for **c** dry and saturated flows and **d** wet flows against the normalised flow height h/δ, where data after the peak flow height of each tested flow are plotted. Dry flows and saturated flows have varying source volume and fixed water content while wet flows have fixed source volume and varying water content
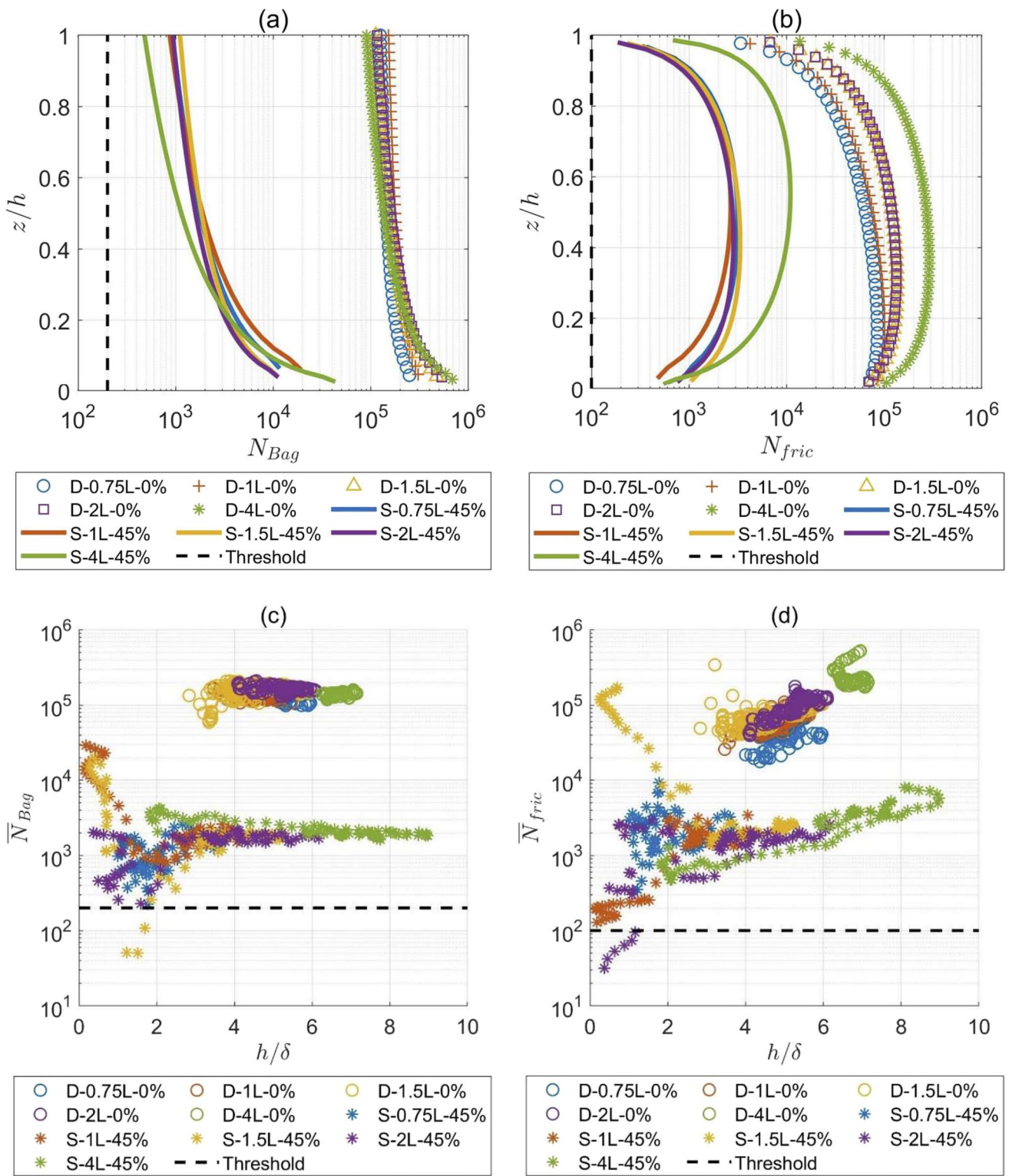
Fig. 10 Local values of **a** Bagnold number (N_{Bag}) and **b** friction number (N_{fric}) against the normalised flow height z/h for dry and saturated flows with varying source volume and fixed water content, where the profile at the peak flow height for each test is plotted. Mean values of **c** Bagnold number ($\overline{N}_{Bag}$) and **d** friction number ($\overline{N}_{fric}$) across the depth against the normalised flow height h/δ for dry and saturated flows, where data after the peak flow height of each tested flow are plotted

Except for the flow tail ($h/\delta \leq 2$) where data are less reliable, $\overline{N}_{Bag}$ and $\overline{N}_{fric}$ are both above their threshold values, hence the effect of viscous shear within the saturated flow surge cannot surpass that of solid contacts in small-scale granular flows.

3.6 Runout behaviour and bulk flow mobility

Deposit geometries are presented in Fig. 11, in which each solid circle in the same colour as the deposit outline represents the Centre of Mass (COM) of the deposit and the horizontal scale is five times the vertical scale. The D test series gives typical dry granular flow morphologies (e.g. Coombs [23], Smith, et al. [38], Bryant, et al. [39], Cheng, et al. [40],

Li, et al. [41]) that shape as backward-sloping heaps with the majority of grains leaning against the slope. In contrast, the deposits of the saturated flows form forward-trending heaps where the majority of grains concentrate near the distal end of the deposit. When the source volume becomes larger, the deposits of dry and saturated flows both grow thicker but develop differently: with larger source volume, the COM of dry flow slightly shifts closer to the slope whereas that of saturated flow moves significantly farther towards the outlet of the horizontal channel. The morphological evolution pattern with water content is exhibited by the deposit shapes of wet flows. When $w < 0.1$, the deposit of a slightly-wetted flow forms a backward heap towards the slope, similar to that of a dry flow; from w between 0.1 and 0.3, the COM

Fig. 11 Deposit outlines of **a** dry and saturated flows (0.45 water content) with different source volumes, and **b** wet flows (2L source volume) with different water content; solid circles represent the centre of mass of each deposit geometry. The horizontal scale is five times the vertical scale
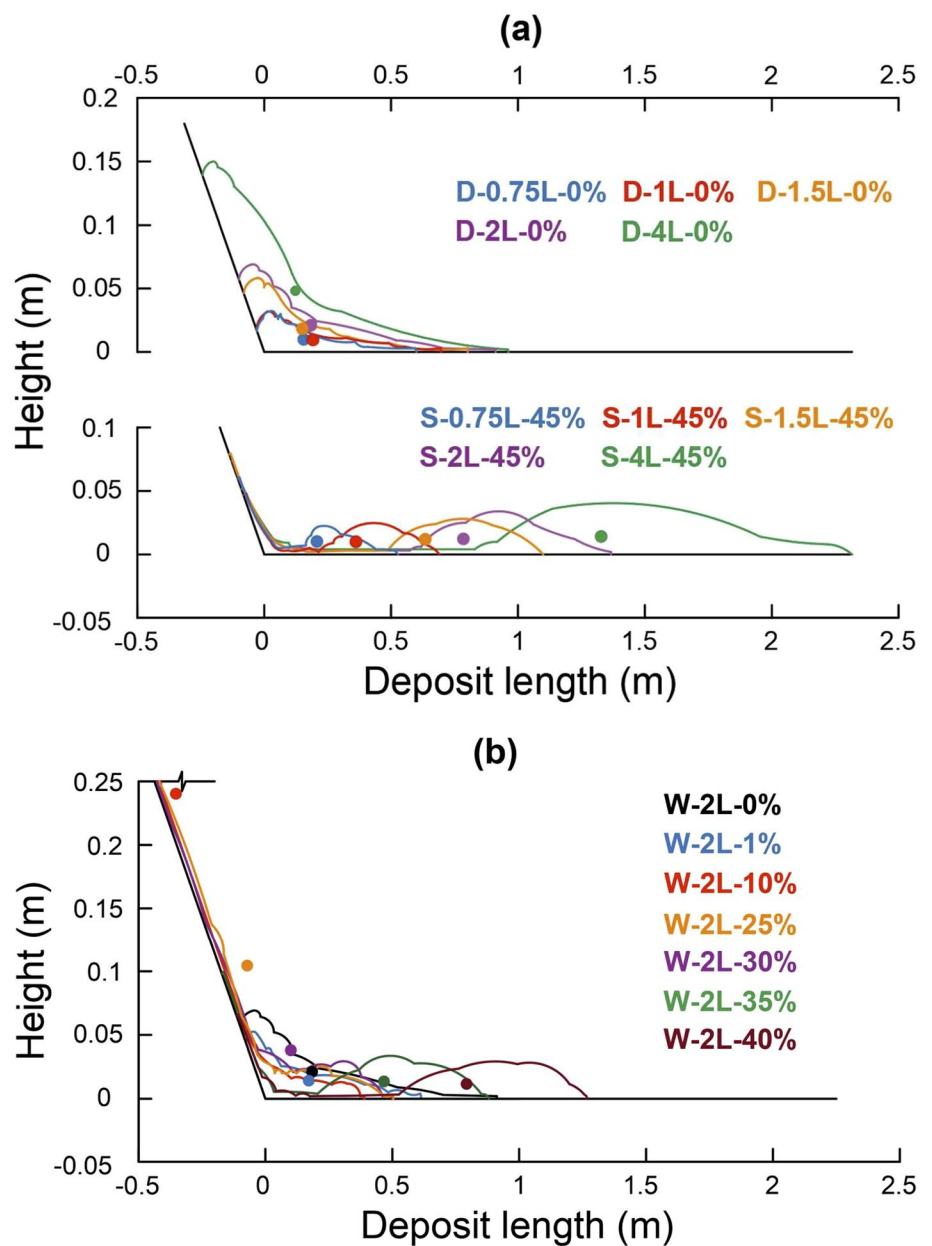
positions demonstrate that most of the flow material is stuck on the slope and that more water tends to allow more grains to flow into the runout channel; after w of 0.3—0.35, a heap composed of most of the grains is formed in the runout channel similar to the saturated deposits, moving further with higher water content. Overall, the evolving water content seems to gradually rather than abruptly mobilise more flow material, from holding most grains on the slope when the flow is highly unsaturated to pushing the majority of solids into the horizontal channel when saturated.

Profiles of travel distances and travel angles presented in Figs. 12 and 13 summarise how bulk flow mobility is influenced by source volumes and water content. The growth in source volume increases the travel distance by a small amount but slightly decreases the travel angle of dry granular flows; we interpret this as a larger volume of dry grains having the potential to spread further in the horizontal channel while a larger proportion of grains are blocked before reaching the inclined flume end. In contrast, the increase in source volume of saturated granular flows significantly increases the travel distance and reduces the travel angle. For
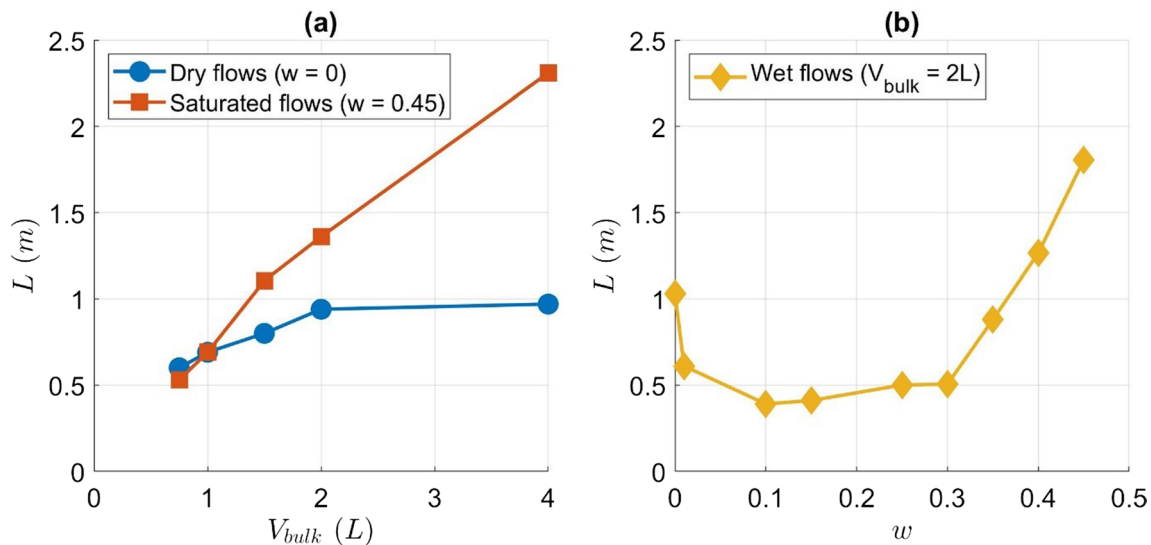
Fig. 12 Travel distance (L) contrasts among **a** tests with varying source volume (dry flows and saturated flows of 0.45 water content) and **b** tests with varying water content (wet flows of 2L source volume)
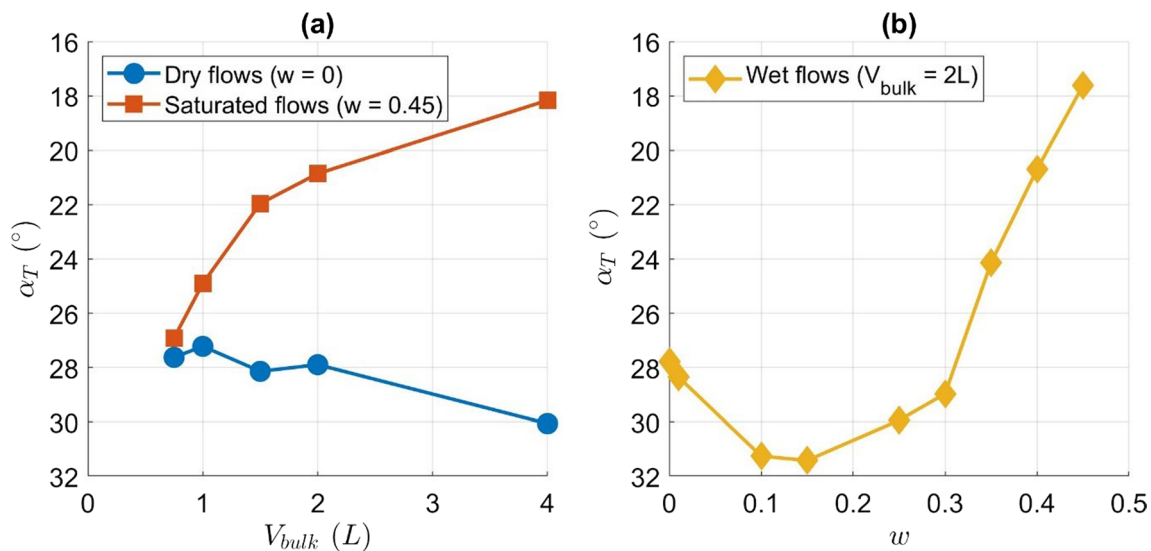
Fig. 13 Travel angle (α_T) contrasts among **a** tests with varying source volume (dry flows and saturated flows of 0.45 water content) and **b** tests with varying water content (wet flows of 2L source volume). α_T axes are reversed to give comparable plots with L curves

wet flows with different water content, bulk flow mobility first drops at an almost-dry condition ($0.01 < w < 0.1$) before slowly growing between $0.1 < w < 0.3$, then approximately linearly growing with moisture content after $w > 0.3$. The result is that a relatively low water content, $w \leq 0.3$ (just above the static saturation value of 0.256) produces lower flow mobility than that of a dry flow at the identical source volume of 2L, while high water content gives higher mobility, with a minimum mobility found around $w = 0.1$.

The effect of water content on bulk flow mobility is also controlled by source volume as shown in Fig. 14, where data of wet flows with different source volumes and water content are plotted against the travel distance ratio, L_{wet}/L_{dry}, which is the travel distance of wet flows normalised by that of dry flows at the identical source volume. Data from the same source volume roughly collapses onto a straight line and the lines approximated from increasing volumes have similar slopes but larger intercept; the applicable linear approximations in Fig. 14 agree with the close-to-linear profiles displayed in both Figs. 12b and 13b when moisture content is relatively high ($w > 0.3$ for 2L tests). A larger source volume gives a longer travel distance at the same water content and makes it easier for wet flows to surpass dry flows in flow mobility. If we define a "boundary water content" denoted by w_x where wet flows would produce the same mobility as the dry flow for a given volume, we see that w_x consistently decreases with source volume. Thus wet granular flows with larger source volumes require a lower water content to

Fig. 14 Travel distance ratios of wet flows to dry flows (L_{wet}/L_{dry}) against water content, where discrete data points in the same colour and sharing the fitted line represent wet flow tests with the identical bulk solid volume. The black dotted line at $L_{wet}/L_{dry} = 1$ denotes where the travel distance of a wet flow equals that of a dry flow at the identical source volume

produce the positive influence (high mobility) of fluid presence, which has ramifications for both the behaviour of field scale events and of scaling debris flows.

4 Discussion

4.1 Shear mechanism

Previously, Fig. 3 showed individual velocity profiles for the different flow constituents – from dry through to saturated and volumes, from small to large for the surge head. In Fig. 15a, following Li, et al. [41], an approach to summarise these outcomes is established to quantitatively describe the velocity profile shape across the different tests. We employ two parameters (16),

(i) the velocity gradient, u_{slip} / u_{ave}, and
(ii) the boundary velocity ratio, $\beta = (u_{ave} - u_{slip}) / (u_{surf} - u_{ave})$,

where slip velocity is u_{slip}, depth-averaged velocity is u_{ave} and surface velocity is u_{surf}. β is also the exponent of the "relaxed" form of the Bagnoldian velocity profile [42], which is given as:

$$u\left(\frac{z}{h}\right) = u_{slip} + (u_{surf} - u_{slip}) \cdot \left[1 - (1 - \frac{z}{h})^{\beta}\right] \tag{8}$$

A larger value of velocity gradient indicates a smaller difference between these two velocities, i.e. a steeper secant line which is related to less internal shearing. The boundary velocity ratio β describes which boundary velocity is closer to the depth-averaged velocity; the value of this ratio approaches 0 when the velocity curve is more vertical in the lower portion of the flow, equals 1 when the velocity profile forms a straight line across the depth, and approaches infinity when the depth-averaged velocity approximates surface velocity. Figure 15b illustrates some examples of the analytical velocity profile where the exponent $\beta = 2$, 3 and 4, assuming a basal slip of $u_{slip}/u_{ave} = 0.5$; the profiles of W-2L-1% and W-2L-40% from Fig. 3f are also plotted as benchmarks.

The coordinate plane of these two parameters, where the velocity profile shapes corresponding to positions in the plane are illustrated, is presented in Fig. 16a; distribution ranges of velocity profile shapes during the main surge part of all tested flows are given in Figs. 16b and 16c, where data points for each test are taken every 5% of the main surge duration starting at the time corresponding with the peak flow height. Peak flow height values are indicated separately. As a reference, the calculated results of the Bagnoldian velocity profiles for dry uniform granular flows with both
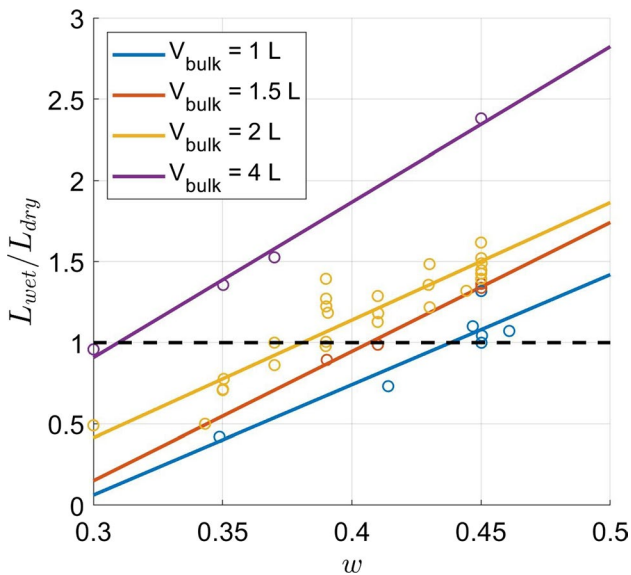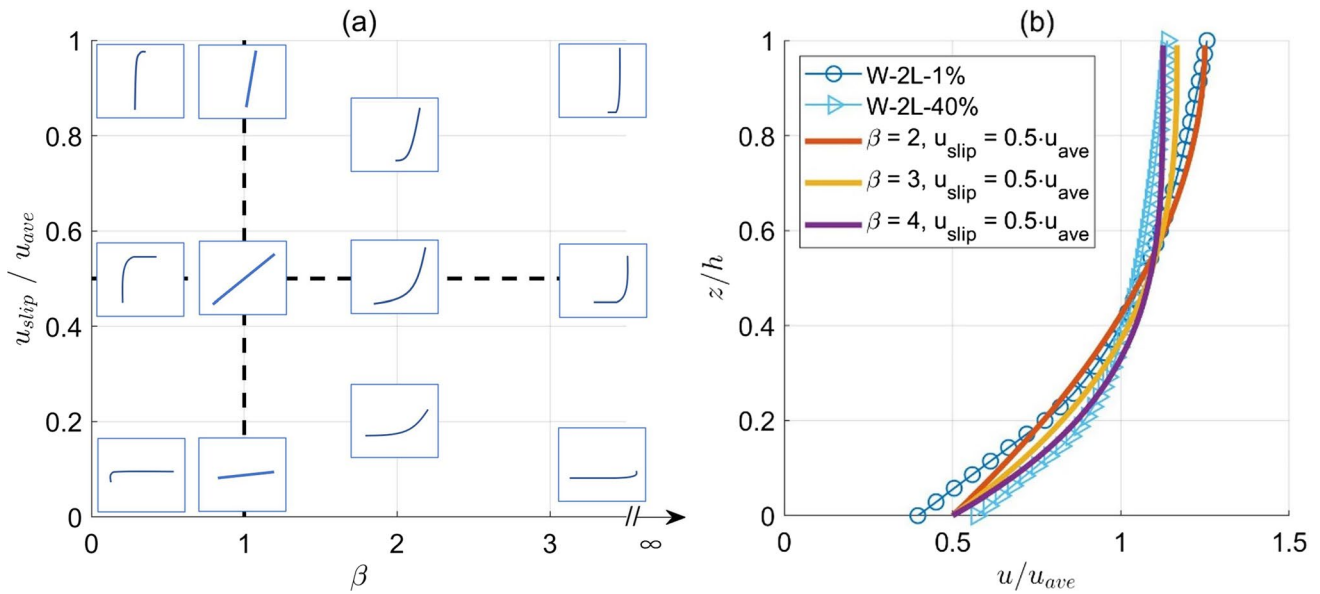
Fig. 15 **a** Schematic diagram of all the velocity profile shapes and their corresponding locations in the coordinate plane of two parameters, i.e. the velocity gradient, u_{slip}/u_{ave}, and the boundary velocity ratio, β). **b** Examples of the theoretical velocity profiles where $\beta = 2$, 3 and 4, in contrast with the profiles at the peak flow height of 2L wet flows with 0.01 and 0.4 water content
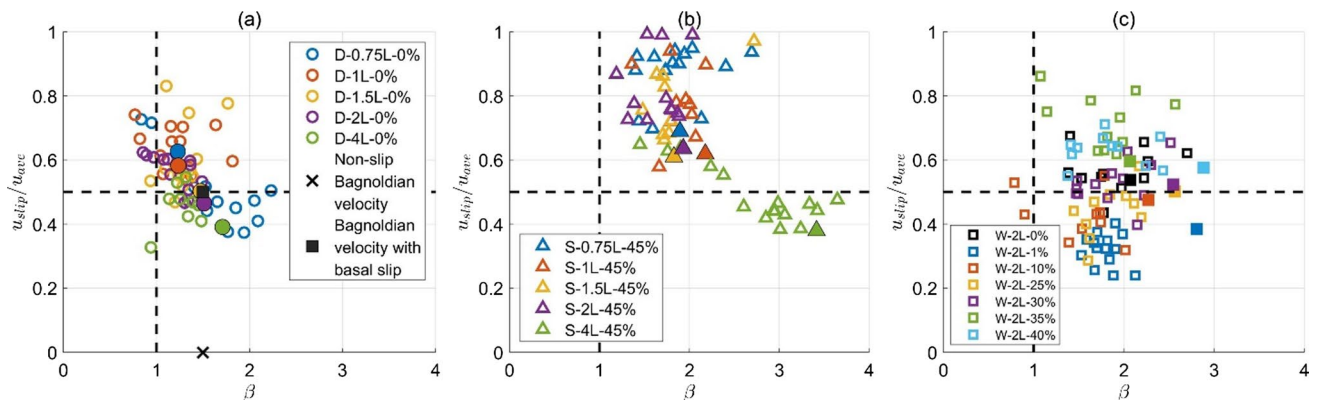

Fig. 16 The distribution range of velocity profile shapes of **a** dry flows with different source volumes, **b** saturated flows with different source volumes (0.45 water content) and **c** wet flows with different water content (2L source volume), where each test contains 10 data points spaced with 10% of the main surge duration. For each test, solid marks represent the data point closest to the maximum flow height, while hollow marks denote data points from the other parts of the flow. The shape of Bagnoldian velocity profiles for steady-uniform dry granular flows both with and without basal slip are given in subplot (**a**)

non-slip and slip boundary conditions are also plotted in Fig. 16a.

Shear mechanisms of granular flows are reflected by the shape distribution of velocity curves. Dry granular flows of smaller volumes tend to shear more uniformly throughout the depth since velocity profiles produce relatively steep straight lines; while for larger volumes, greater differences occur between depth-averaged and slip velocities, showing that shearing tends to be more limited to the flow-bed boundary. Velocity shape evolution in response to the increased source volume for saturated flows is similar to that of dry

flows but the velocity profiles are more curved, showing that the upper portion of the flow develops less velocity difference whereas the basal layer is subjected to stronger shear; thus the participation of saturating pore fluid weakens the global shear trend across the flow depth and reinforces the localisation of shear movement, allowing the upper portion of the flow to more easily move as a whole. With increasing water content, a nearly-vertical upward shift is demonstrated by wet flows in Fig. 16c, in which velocity gradient increases while β changes little; hence a higher water content allows

the grains near the bottom to keep up with those in the upper part.

There are some overlaps in data, particularly in the oversaturated flows. For example, examining the velocity profiles at the flow head (maximum height, Figs. 3c and 3f), the 40% curve has a similar slip velocity (and normalized velocity) as the 35%, but the upper part is more vertical at larger values and thus its averaged velocity is larger. Similar (or only slightly larger) u_{slip} and notably larger u_{ave} lead to lower u_{slip}/u_{ave}, and a more vertical profile means a larger β value. So while the general trend is an increase in basal slip with increasing water, between 35 and 40% the more impactful change is lessened shear in the upper part of the flow (i.e. increase in β).

An increase in water content results in a clear trend of lessening of shear throughout the depth. With velocity profiles for saturated flows that are similar to that of plug flow (Fig. 3e, f), this appears to support the depth-averaged continuum assumption commonly applied to gravity-driven flows. Since the velocity loss between translational granular layers results more from solid friction ($\overline{N}_{fric}$ in Fig. 10is almost always above its threshold), the lessened intergranular shear indicates that the fundamental role of pore fluid in granular flows is to reduce the solid friction by lubrication and buoyancy. Combined with the observation that differences in depth-averaged velocities only occur in wet flows (Fig. 4), it can be surmised that, where flow velocity is independent of source volume (dry flows), this is due to strong and constant solid friction, while the loss of solid friction due to the participation of pore fluid is the key to the efficient increase of flow velocity with both water content and volume in wet flows.

4.2 Surge velocity, pore pressure and bulk flow mobility

Hungr, et al. [43] showed that for a given field catchment, there is a simple relationship between the exit velocity of debris flow within a confined reach and the runout on the fan – that is, that the square of the velocity linearly correlates to the runout length. This was explored for lab-scale experiments in [37]. Following this, Fig. 17 presents the depth-averaged front flow velocity u_{ave} at the lower position near the end of the slope against (a) the deposit travel angle and (b) the runout length for all flows. A clear relationship exists for both, with Pearson correlation coefficients of 0.95 and 0.89, respectively. This indicates that the deposition phase of these experimental granular flows, like debris flows in the field, is essentially set by the condition established at the end of the slope or final reach of the flow.

The link between velocity, pore pressure and runout is further shown in Fig. 18 for the wet flows, where a clear correlation is found between (a) depth-averaged front flow velocity u_{ave}, (b) maximum absolute pore pressure, whether positive or negative and (c) deposit travel angle. Thus cohesion or matric suction occurring in unsaturated flows is related to the reduction of velocity compared with dry flows, and the positive pore pressures developed due to saturation of higher moisture content flows to velocity enhancement. Thereafter, the mobility is intrinsically related to the depth-averaged velocity of the surge, as previously seen in field-related work [43].

As shown in Fig. 17, in the low water content range ($w \leq 0.3$) where cohesive forces dominate, the flow velocity and mobility are lower. Bulk mobility therefore does not monotonically increase with water content but has a minimum between $w = 0.1$ and 0.15 – see also Figs. 13b and 14b. This behaviour has also been observed by Zhou, et al. [12], in which the effect of matric suction and the resultant increased shear strength of unsaturated flow material is used to explain this minimum mobility; the evolution of shear mechanism with water content, which shows an increasingly weakened bulk shear (Fig. 15c), appears to support this explanation. Conversely, the decrease in bulk flow mobility can be alleviated when the shear strength is reduced by the reduction or disappearance of the matric suction stress due to the saturation of the flow material; evidence can be found in Fig. 7b and Fig. 8b, where positive pore pressure starts to occupy a larger space above the time axis than negative values after reaching $w > 0.3$ which is also the water content at which pore fluid starts to spill out from the flowing granular body. The relationship between travel angle and water content beyond $w > 0.3$ presented in Fig. 18c is approximately linear (see also Figs. 12b and 13b), given the conditions of a smooth bed, 2D flow path and negligible relative negative pore pressure.

Previously in Fig. 14, the boundary water content w_x necessary for the wet flows to exceed the runout distance of dry flows for the same volume was found to decrease with volume and, as suggested in Fig. 18, a prevalence of negative pore pressure must occur below w_x. We also note that the saturation water content w_0 was found to be 0.256 for a static average packing of the material, while the lowest value of w_x for the 4L test is 0.31, i.e. above that of the static packing. Therefore, we may deduce that larger granular flows more easily keep saturated in motion for several linked reasons. The expansion of internal pore volume and resulting desaturation of the flow due to dilation during downslope motion is limited for larger volumes by an increasing flow depth (hence, increase in total stress), as the
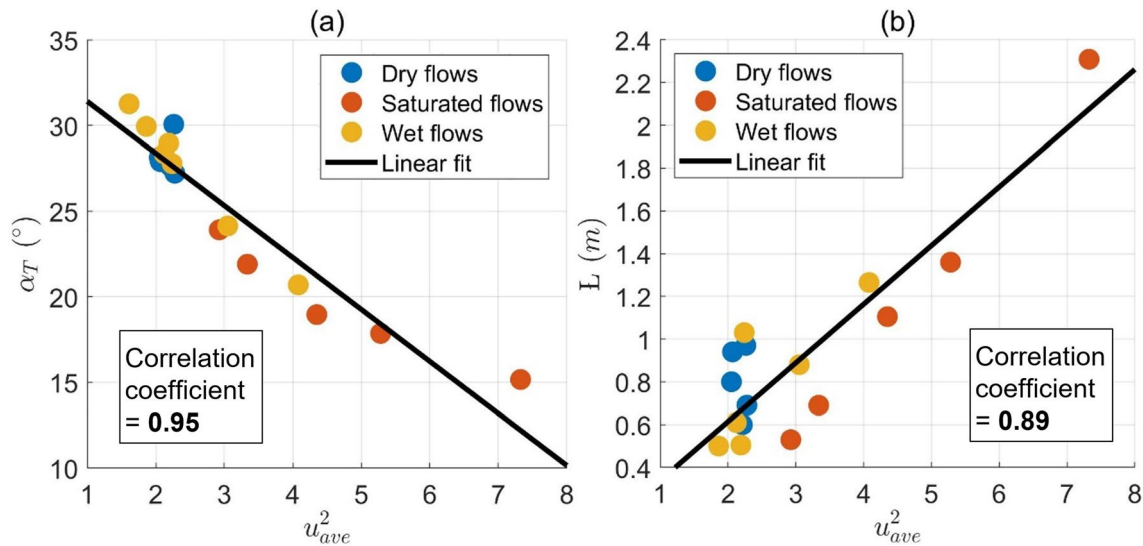
Fig. 17 Correlation between the square of the downslope depth-averaged velocity (u_{ave}) taken at the maximum flow height against **a** travel angle (α_T) and **b** travel distance (*L*)
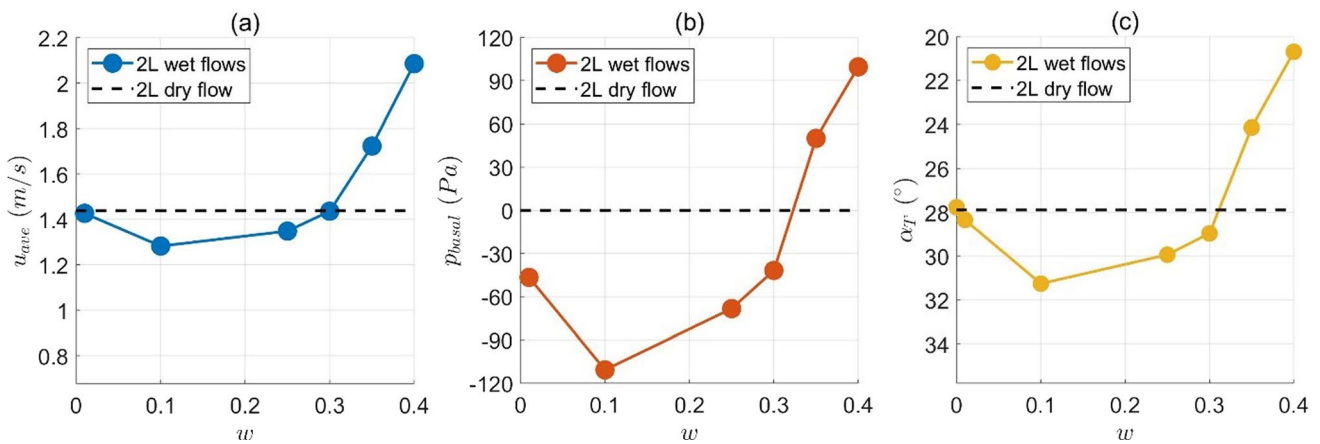

Fig. 18 Similar evolution patterns against water content for **a** depth-averaged velocity (u_{ave}) at the peak flow height, **b** the downslope (100mm from the flume end) basal pore pressure (p_{basal}) at its abso-lute maximum and **c** the reversed travel angle (α_T). Note that the saturation water content for static sample is 0.256

negative pore pressure occupies less space on the time axis in response to an increased total stress, particularly at the flow base (Fig. 7a). This leads to solid enduring contacts being strengthened for thicker flows ($\overline{N}_{fric}$ increases with h/δ in Fig. 10) and grains separating less from each other, and hence to greater plug-type behaviour and larger slip velocities for larger volumes. Moreover, the absence of excess pore pressure in all tested flows (Fig. 7) implies that the high

mobility of saturated granular flows does not result from excess pore pressure per se, but can be achieved by fluid buoyancy and mitigation of intergranular effective normal stress σ', defined as the difference between the intergranular normal stress and pore fluid pressure. The addition of excess pore pressures in granular flows may result in even greater mobility via a greater reduction in σ', but this should be considered as being on a continuum of general behaviour.

5 Conclusions

To investigate pore fluid effects on granular flow behaviours, a series of small-scale experiments employing 3.85 mm uniform solid ceramic particles has been conducted in a narrow smooth-bottomed tilted flume, with test conditions varying in source volume and water content. Transducer signals, PIV-processed high-speed images and deposit measurements were used to analyse the internal dynamics and bulk flow mobility of granular flows ranging from dry to oversaturated. The following conclusions are made:

(i) Pore fluid pressure shows a continuous influence on granular flow behaviours from matric suction to buoyancy in response to the transition of water content from dry to oversaturated. The head velocity and flow mobility of wet flows are smaller than those of dry flows with the equivalent source volume when cohesion or matric suction dominates the unsaturated flow surge at low water content (hence flow mobility is effectively reduced), but are greater than those of dry flows when pore pressure is mostly positive in the saturated flow surge at high water content (hence flow mobility is effectively enhanced). Similar profiles against water content can be found among the depth-averaged velocity (u_{ave}) at peak flow height, basal pore pressure (p_{w}) at absolute maximum and travel angle (α_{T}) of the deposit for granular flows in the identical source volume: the mobility determined by travel angle for retarded flows varies gradually with water content, with a minimum value occurring when the flow is slightly-wetted rather than fully dry, whereas for enhanced flows, α_{T} grows approximately linearly at a steeper gradient with water content.

(ii) Above a given transition point when matric suction no longer dominates, wet flows at different volumes have similar close-to-linear increasing patterns of travel distance against water content. However, a larger source volume leads to higher bulk flow mobility at the same water content. Defining a "boundary water content" (w_{x}) for wet flows, in which the resultant travel distance is identical to the dry flow at the same volume, we find that this decreases with the source volume; i.e. wet flows at very large volumes (field-scale flows for instance) are less likely to produce shorter runout than dry flows, even at very low water content. This may be due to the increased flow thickness inhibiting the bulk dilation of flow material during downslope motion and hence, the desaturation process. Therefore, for larger or thicker flows, the pore space expands less during downslope movement and negative pore pressures are reduced in the flow surge.

(iii) For wet granular flows with different water content, the momentum transfer mechanism varies consistently with flow thickness. In thicker flows, mean values of Savage number and Bagnold number across the flow depth are lower and those of friction number are higher, indicating an increasing level of solid friction and decreasing solid inertia. Viscous fluid shear increases with water content, as mean values of Bagnold number and friction number both drop.

(iv) As seen for in field scale scenarios, a linear relationship can be established for highly idealised granular flows between the square of the depth averaged velocity near the slope transition and mobility as measured by both travel angle and runout. For dry to oversaturated flows at one volume, further relationships are established between velocity, pore pressure and travel angle, which highlights the role of pore pressure in promoting flow mobility.

(v) The fundamental effect of pore fluid that is sufficient to saturate the flow surge is to reduce the solid frictional interactions within granular flow. The mitigation of intergranular friction causes the local velocity difference between grains of neighbouring layers to decrease and the flow throughout the depth to move more as an ensemble. Velocity profiles of dry flows show relatively uniform shear across the flow depth; while those of wet flows may approach a "plug-flow" shape: the upper portion of the flow tending to move as a block, particularly at a larger source volume, separate from the bottom granular layer. A greater slip velocity also results from higher water content. This may suggest that wet flows, especially saturated flows, are more suitable for the assumption of continuum flow. In addition, we did not find notable excess pore pressure in any of the tests, even when a clear increase in bulk mobility was presented. This indicates that the effect of excess pore pressure, which plays a significant role in field-scale geophysical flows, should be considered as leading to a further reduction of intergranular contacts or effective stress, rather than being an a priori necessity to produce high bulk flow mobility.

Appendix

Velocity profile processing

Figure A1 shows a screenshot of "static mesh" GeoPIV software [44] on a scale of 1 mm = 4.41 pixels, where an interrogation window (i.e. patch) and the stationary mesh at the "downslope position" are highlighted. The patch size is 24 × 24 pixels (1.4δ), which gives approximately 2 grains per patch. The PIV mesh consists of 4 columns of patches, spaced at 12 pixels (1/2 patch size) along the x-direction and 2 pixels (1/12 patch size) along the z-direction; the mesh covers from at least one patch below the bed to at least half a patch above the observable surface of the flow peak to accurately detect the bed and surface position.

An example of the velocity profile derived from PIV analysis of the W-2L-40% test is given in Figure A2, showing details of the postprocessing of velocity profiles. First, each velocity curve at a given moment is averaged from the instantaneous velocity profiles over 0.02 s. Second, the flow surface is identified where the maximum velocity occurs and data above the flow surface are deleted; note that if the height of the maximum velocity data is below the flow surface detected by the ultrasonic sensor, the velocity data are kept until reaching the sensor-detected surface; this flow surface that considers both PIV and sensor measurements then determines the flow height at each instant of time. Next, velocity profiles are fitted by power functions to reduce local velocity noise which can magnify the variation in the derivative local shear rate. Then the velocity data below the "basal patch centre", i.e. the centre of the patch touching the flume bed (Figure A1), need to be amended because the stationary subimage of the flume bottom can lead to velocity underestimation and the measured data below half a grain size at the bottom, i.e. $h = \delta/2 = 1.93$ mm, are not "real" as they should be constant for the measurement taken over the same particle. The data below the basal patch centre of a fitted velocity curve are replaced by a straight line with a uniform velocity gradient which equals that between the data point at the basal patch centre and the one above it; by eye observation and hand calculation, the basal grain velocity related to the velocity curve in Figure A2 is around 1.02 – 1.35 m/s, close to the estimated slip velocity. The amended power-fitted velocity profiles at the front, middle and rear parts of the W-2L-40% flow surge are compared with the actual velocity curves averaged over 0.02 s and the original instantaneous velocity profiles within this time range in Figure A3, giving generally satisfactory fitting results above the basal patch centre.
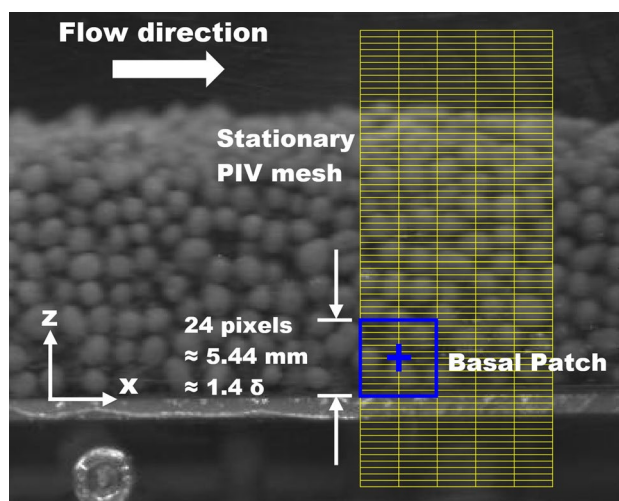
See Figs. 19, 20 and 21.

Fig. 19 Schematic diagram of PIV analysis, where a typical patch denoted with a blue square and the stationary PIV mesh in yellow are highlighted
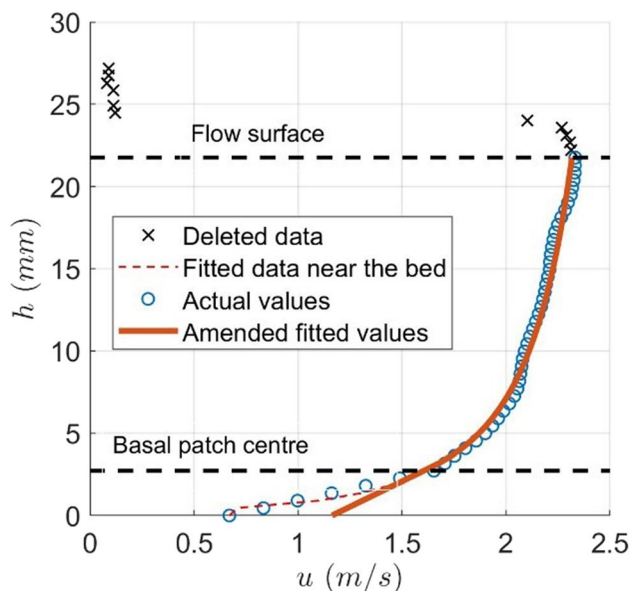

Fig. 20 Example of velocity profile showing the original data from PIV analysis and the processed data fitted by a power function

Bulk flow mobility quantification

Travel angle is the main parameter used to compare bulk mobilities of different tests, as the position of the COM is affected by both external and internal energy dissipation; while travel distance directly shows the spreading range of the granular mass, and is of relevance at field scale to the hazard posed by landslides. Travel distance is obtained by measuring the length of deposit after every test. Travel distance of wet granular flows can easily be identified as the
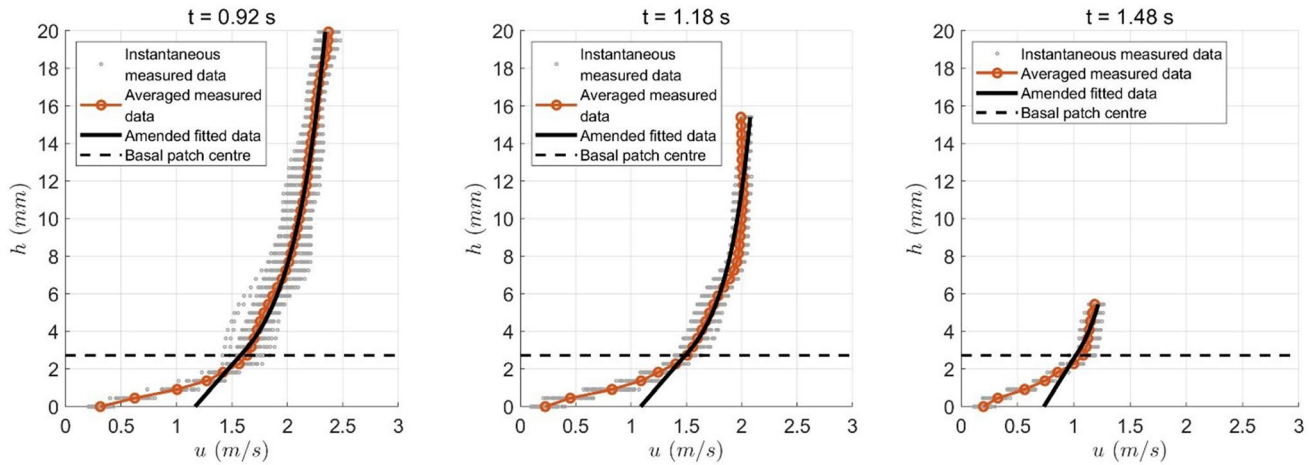
Fig. 21 Comparisons between the instantaneous actual velocities, averaged actual velocities, and power-fitted velocities with data below the basal patch centre amended; instantaneous velocity profiles are taken over 0.02 s around the front (t=0.92 s), middle (t=1.18 s) and rear (t=1.48 s) of the flow surge, whereas the averaged velocity profiles are derived from the same 0.02 s range

outer margin of the deposit is distinct at the distal end; the deposits of dry flows, on the other hand, are more scattered near the leading edge, hence the boundary of the deposit body is determined by a transversal line consisting of 15 grains, where grains approximately occupy half the channel width (Figure B1a). Travel angle is determined by the initial and final COM positions. The final COM position is calculated from the deposit side-view geometry, which is recorded by video and is then drawn in drafting software; different frames are taken from the video and for each frame only the central part of the image is kept to reduce the error due to perspective distortion; the 2×2 mm grid as shown in Figure B2 ensures the drawn outline matches the deposit shape. For the calculation of travel angle, use of the initial COM position inside the hopper will result in an inaccurate value as the initial piling height of grains is irrelevant to the flowrate out of the hopper gate due to granular arching [45]. Instead, considering that discrete free-falling particles densify when hitting a fixed plane [46], the flow motion can be regarded as initiating on the bed at a position directly below the hopper gate; therefore, the source material can be approximated into a block with its top surface parallel to the hopper gate and its bottom side touching the flume bed, as shown in Fig. 2a.

See Figs. 22, 23.

Fig. 22 Schematic illustrations of **a** determining the range of dry flow deposits, where the red line divides the deposit body from scattered individual grains and **b** drawing deposit outlines from video frames
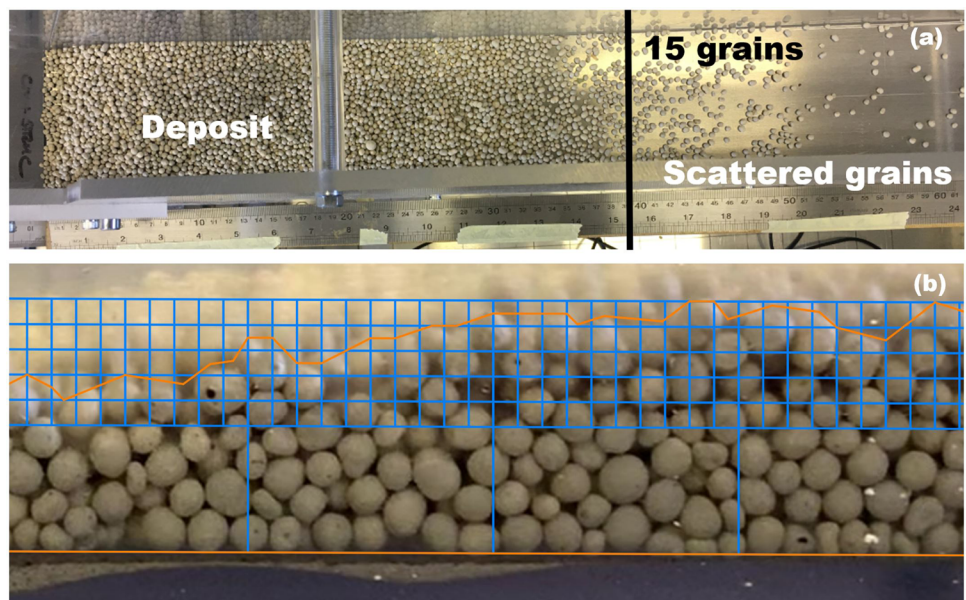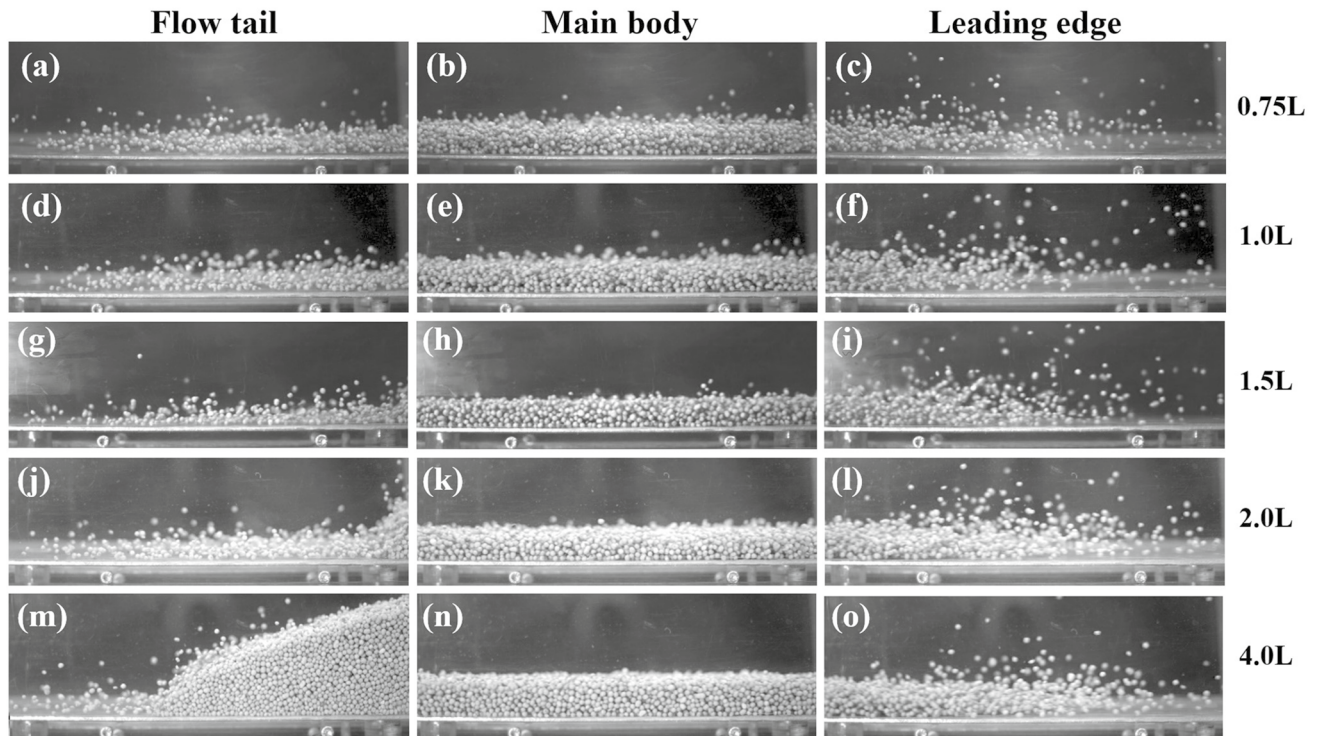
Dry granular flows (0 water content)

Fig. 23 Camera-captured side-view profiles of dry granular flows. Five rows represent different utilised source volumes from 0.75L to 4L, while three columns respectively represent the flow tail, main body and leading edge of each tested dry flow. The granular piles appearing in subplots (**j**) and (**m**) show that the upstream end of the flow deposit has extended to more than 100 mm from the inclined flume outlet

Flow profiles

To give plain and straightforward impression of different granular flows in our small-scale flume experiments, the flow profile for each tested flow recorded by high-speed camera pointing at the flume sidewall are demonstrated in Figure C1-C3, where three columns of subplots, from left-hand side to right-hand side, show the flow tail, main flow body and leading edge of the tested flow, while different rows represent the flows with different values of the test variable (i.e. source volume for dry and saturated flows whereas water content for wet flows). With a larger source volume, granular flow becomes thicker and produces less saltated grains at the free surface and in the leading edge. Dry flow can lead to the deposit accumulating from the runout channel to the inclined flume so that the larger-volume granular pile extends further backward (i.e. towards the upstream direction); for saturated flows, on the other hand, the majority of grains can always flow into the horizontal channel. Similar circumstance also occurs for wet flows with varying water content. At a low water content (e.g. $w = 0.1 - 0.3$) grains in the flow tail part tend to come to rest in the inclined flume; unlike the backward accumulation of dry grains, this is mainly due to cohesion or matric suction applied to the basal boundary of the flow. When water content exceeds 0.3, however, the influence of matric suction fades with the increased amount of pore fluid and grains are no longer stuck on the flume bed.

See Figs. 24, 25.

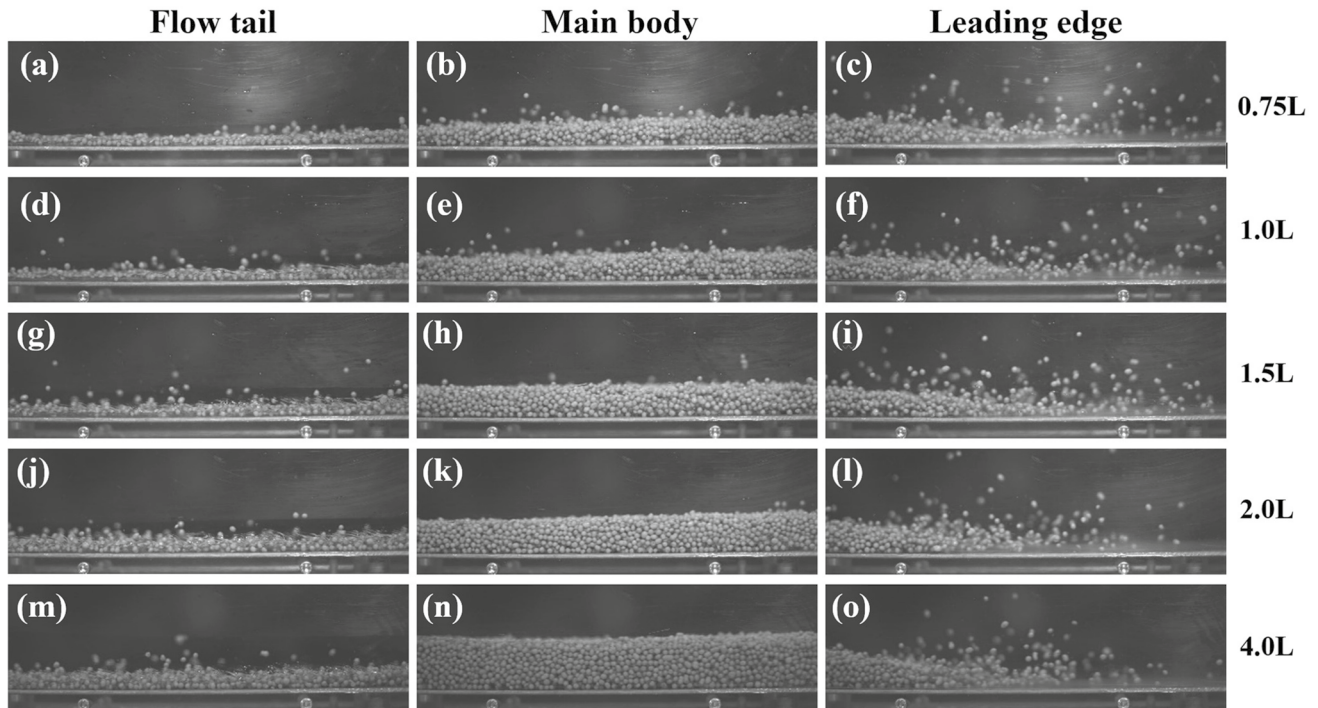## Saturated granular flows (0.45 water content)

Fig. 24 Camera-captured side-view profiles of saturated granular flows with fixed 0.45 water content. Five rows represent different utilised source volumes from 0.75L to 4L, while three columns respectively represent the flow tail, main body and leading edge of each tested dry flow
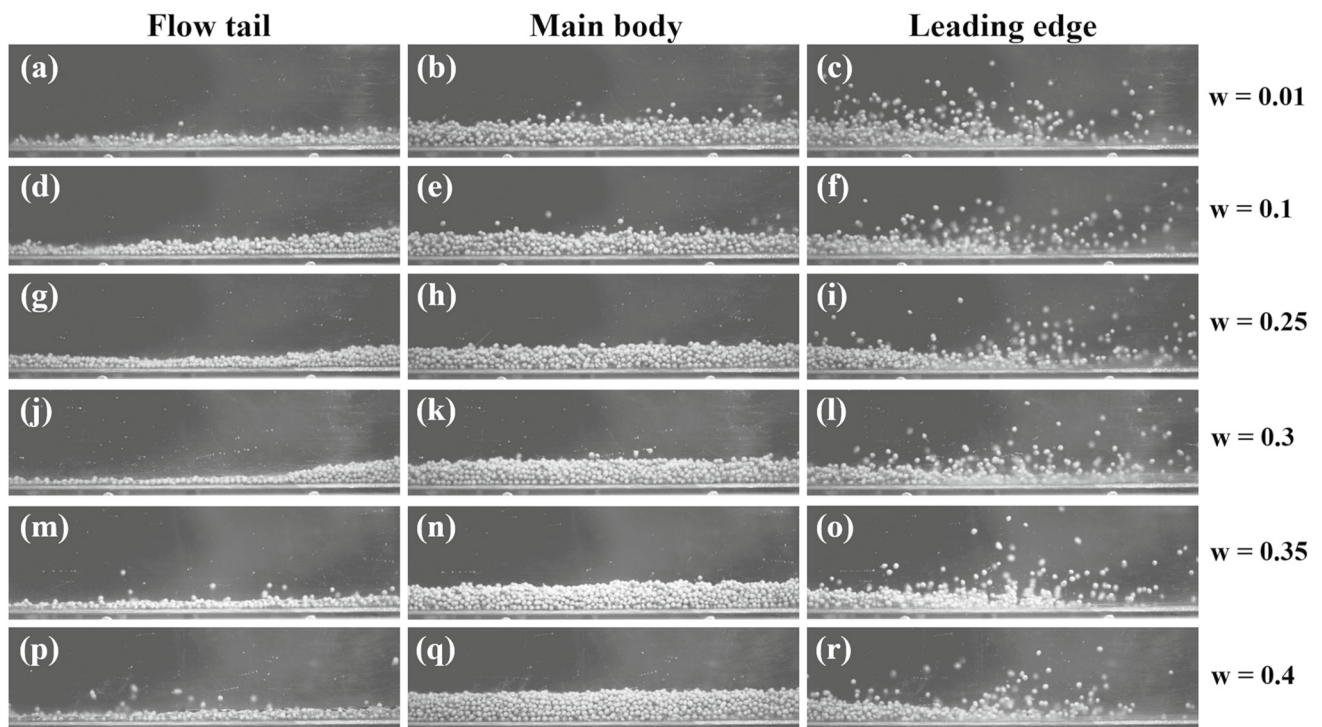
Wet granular flows (2L source volume)

Fig. 25 Camera-captured side-view profiles of wet granular flows with a fixed 2L source volume. Six rows represent different utilised water content from 0.01 to 0.4, while three columns respectively represent the flow tail, main body and leading edge of each tested dry flow. Static grains without saltation in subplots (**d**), (**g**) and (**j**) show that grains are stuck on the inclined flume bed before flowing into the horizontal channel

Declarations

References

1. Louge, M.Y.: Model for dense granular flows down bumpy inclines.". Phys. Rev. E **67**, 061303 (2003)

2. MiDi, G.D.R.: On dense granular flows. Eur. Phys. J. E **14**(4), 341–365 (2004)

3. Jop, P., Forterre, Y., Pouliquen, O.: A constitutive law for dense granular flows. Nature **441**(7094), 727–730 (2006)

4. Kumaran, V.: Dense granular flow down an inclined plane: from kinetic theory to granular dynamics. J. Fluid Mech. **599**, 121–168 (2008)

5. Gray, J.M., Timm, N., Gajjar, P., Kokelaar, P.: Particle-size segregation in dense granular avalanches.". Comptes Rendus Physique **16**, 73–85 (2015). https://doi.org/10.1016/j.crhy.2015.01.004

6. Fredlund, D.G., Ro Morgenstern, N., Widger, R.A.: The shear strength of unsaturated soils.". Can. Geotech. J. **15**, 313–21 (1978)

7. Pierrat, P., Caram, H.S.: Tensile strength of wet granula materials.". Powder Technol. **91**, 83–93 (1997)

8. Vanapalli, S.K., Fredlund, D.G., Pufahl, D.E., Clifton, A.W.: Model for the prediction of shear strength with respect to soil suction.". Can. Geotech. J. **33**, 379–92 (1996)

9. Jarray, A., Magnanimo, V., Luding, S.: Wet granular flow control through liquid induced cohesion. Powder Technol. **341**, 126–139 (2019)

10. Pailha, M., Pouliquen, O.: A two-phase flow description of the initiation of underwater granular avalanches. J. Fluid Mech. **633**, 115–135 (2009)

11. Tognacca, C., and Minor, H.-E.: Role of surface tension, fluid density and fluid viscosity on debris-flow dynamics. Paper presented at the Second International Conference on Debris-Flow Hazards Mitigation: Mechanics, Prediction and Assessment, (2000).

12. Zhou, G., Wright, N.G., Sun, Q., Cai, Q.: Experimental study on the mobility of channelized granular mass flow.". Acta Geologica Sinica - English Edition **90**(3), 988–98 (2016). https://doi.org/10.1111/1755-6724.12739

13. Andreotti, B., Yoël, F., Olivier, P.: Granular Media: Between Fluid and Solid. University Press, Cambridge (2013)

14. Guazzelli, É., Pouliquen, O.: Rheology of dense granular suspensions. J. Fluid Mech. **852**, P1 (2018)

15. Du, J., Zhou, G.G.D., Tang, H., Turowski, J.M., Cui, K.F.E.: Classification of stream, hyperconcentrated, and debris flow using dimensional analysis and machine learning.". Water Resour. Res. **59**, e2022WR033242 (2023)

16. Iverson, R.M.: The physics of debris flows. Rev. Geophys. **35**(3), 245–296 (1997). https://doi.org/10.1029/97RG00426

17. Kaitna, R., Palucis, M.C., Yohannes, B., Hill, K.M., Dietrich, W.E.: Effects of coarse grain size distribution and fine particle content on pore fluid pressure and shear behavior in experimental debris flows.". J. Geophys. Res.: Earth Surface **121**(2), 415–41 (2016)

18. Kowalski, J., McElwaine, J.N.: Shallow two-component gravity-driven flows with vertical variation.". J. Fluid Mech. **714**, 434–62 (2013)

19. Iverson, R.M., George, D.L.: A depth-averaged debris-flow model that includes the effects of evolving dilatancy. I. Physical basis.". Proceed. Royal Soc. A: Math. Phys. Eng. Sci. **470**, 20130819 (2014)

20. Bouchut, F., Fernández-Nieto, E.D., Mangeney, A., Narbona-Reina, G.: A two-phase two-layer model for fluidized granular flows with dilatancy effects.". J. Fluid Mech. **801**, 166–221 (2016)

21. Kong, Y., Guan, M., Li, X., Zhao, J., Yan, H.: Bi-linear laws govern the impacts of debris flows, debris avalanches, and rock avalanches on flexible barrier. J. Geophys. Res.: Earth Surface **127**, 2022JF006870 (2022)

22. Raymond, G.P.: Reinforced ballast behaviour subjected to repeated load. Geotext. Geomembr. **20**(1), 39–61 (2002)

23. Coombs, S.: A Physical Investigation of the Flow Structure and Mobility Behaviour of Collisional Granular Landslides." Queens University, (2018).

24. Taylor-Noonan, A.M., Bowman, E.T., McArdell, B.W., Kaitna, R., McElwaine, J.N., Andy Take, W.: Influence of pore fluid on grain-scale interactions and mobility of granular flows of differing volume.". J. Geophys. Res.: Earth Surface **127**(12), e2022JF006622 (2022)

25. White, D.J., Take, W.A., Bolton, M.D.: Soil deformation measurement using particle image velocimetry (PIV) and photogrammetry.". Geotechnique **53**(7), 619–31 (2003)

26. Sanvitale, N., Bowman, E.T.: Internal imaging of saturated granular free-surface flows.". Int. J. Phys. Model. Geotech. **4**(12), 129–42 (2012)

27. Gollin, D., Brevis, W., Bowman, E.T., Shepley, P.: Performance of PIV and PTV for granular flow measurements.". Granular Matter **19**(3), 1–16 (2017)

28. da Cruz, F., Emam, S., Prochnow, M., Roux, J.-N., Chevoir, F.: Rheophysics of dense granular materials: Discrete simulation of plane shear flows.". Phys. Rev. E **72**(2), 021309 (2005)

29. Iverson, R.M., Logan, M., LaHusen, R.G., Berti, M.: The perfect debris flow? Aggregated results from 28 large-scale experiments.". J. Geophys. Res.: Earth Surface (2010). https://doi.org/10.1029/2009jf001514

30. Savage, S.B., Hutter, K.: The motion of a finite mass of granular material down a rough incline.". J. Fluid Mech. **199**, 177–215 (1989)

31. Bagnold, R.A.: Experiments on a gravity-free dispersion of large solid spheres in a Newtonian fluid under shear. Proceed. Royal Soc. London Series A Math. Phys. Sci. **225**, 49–63 (1954)

32. Iverson, R.M., Denlinger, R.P.: Flow of variably fluidized granular masses across three-dimensional terrain: 1. Coulomb mixture

theory.". J. Geophys. Res.: Solid Earth **106**, 537–52 (2001). https://doi.org/10.1029/2000jb900329

33. Iverson, R.M., LaHusen, R.G.: Friction in debris flows: inferences from large-scale flume experiments.". Hydraulic Eng. **93**, 1604–09 (1993)

34. Parsons, J.D., Whipple, K.X., Simoni, A.: Experimental study of the grain-flow, fluid-mud transition in debris flows.". J. Geol. **109**, 427–47 (2001)

35. Straub, S.: Self-organization in the rapid flow of granular material: evidence for a major flow mechanism. Geol. Rundsch. **85**(1), 85–91 (1996)

36. Sanvitale, N., Bowman, E.T.: Visualization of dominant stress-transfer mechanisms in experimental debris flows of different particle-size distribution.". Can. Geotech. J. **54**(2), 258–69 (2017)

37. Takahashi, T.: *Debris Flow*. IAHR Monograph Series. Rotterdam: AA Balkema, (1991).

38. Smith, G.M., Davies, T.R., McSaveney, M.J., Bell, D.H.: The Acheron rock avalanche, Canterbury, New Zealand—morphology and dynamics.". Landslides **3**, 62–72 (2006)

39. Bryant, S.K., Andy Take, W., Bowman, E.T.: Observations of grain-scale interactions and simulation of dry granular flows in a large-scale flume.". Can. Geotech. J. **52**(5), 638–55 (2014)

40. Cheng, Y.M., Fung, W.H.I., Li, L., Li, N.: Laboratory and field tests and distinct element analysis of dry granular flows and segregation processes.". Natural Hazards and Earth Syst. Sci. **19**(1), 181–99 (2019)

41. Li, K., Wang, Y.-F., Lin, Q.-W., Cheng, Q.-G., Yue, Wu.: Experiments on granular flow behavior and deposit characteristics: implications for rock avalanche kinematics. Landslides **18**(5), 1779–1799 (2021)

42. Bi, W., Delannay, R., Richard, P., Valance, A.: Experimental study of two-dimensional, monodisperse, frictional-collisional granular flows down an inclined chute.". Phys. Fluids **18**, 123302 (2006). https://doi.org/10.1063/1.2405844

43. Hungr, O., Morgan, G.C., Kellerhals, R.: Quantitative analysis of debris torrent hazards for design of remedial measures.". Can. Geotech. J. **21**(4), 663–77 (1984)

44. White, D.J., Take, W.A.: *Particle image velocimetry (PIV) software for use in geotechnical testing.* University of Cambridge, Department of Engineering, (2002).

45. Janssen, H.A.: Versuche über Getreidedruck in Silozellen/Zeitschr d. Vereines deutscher Ingenieure. **39**, 1045–1049 (1895)

46. Dunatunga, S., Kamrin, K.: Continuum modelling and simulation of granular flows through their many phases. J. Fluid Mech. **779**, 483–513 (2015)